



Hydrogenation of α,β -unsaturated aldehydes over defective UiO-66 with Frustrated Lewis Pairs: Modulation of densities of defect sites via tailoring ligand-vacancies

Linhao Zhong^{a,1}, Xiaoqing Liao^{a,1}, Haishuai Cui^{a,b}, Hean Luo^{a,c,d}, Yang Lv^{a,c,d,e,*}, Pingle Liu^{a,c,d,*}

^a College of Chemical Engineering, Xiangtan University, Xiangtan 411105, China

^b College of Materials and Chemical Engineering, Hunan Institute of Engineering, Xiangtan 411105, China

^c Engineering Research Centre for Chemical Process Simulation and Optimization of Ministry of Education, Xiangtan University, Xiangtan 411105, China

^d National & Local United Engineering Research Centre for Chemical Process Simulation and Intensification, Xiangtan University, Xiangtan 411105, China

^e Anhui Huaxing Chemical Co., LTD., Postdoctoral Research Workstation, Maanshan 243000, China

ARTICLE INFO

Keywords:

Selective hydrogenation
Solid FLPs catalysts
Modulation of defect sites
UiO-66
 α,β -unsaturated aldehydes

ABSTRACT

In this work, defect-rich UiO-66-FA catalysts were synthesized using a modulator-induced defect formation strategy via tailoring ligand-vacancies and applied in the transfer hydrogenation of α,β -unsaturated aldehydes using cyclohexanol as the hydrogen source. The study reveals that the constructed surface defect in UiO-66 promotes the emergence of Zr-OH sites (Lewis base) and the neighboring unsaturated Zr⁴⁺ sites (Lewis acid) on the surface of UiO-66-FA, thereby generating solid Frustrated Lewis Pairs (FLPs) sites. Furthermore, the manipulation of the densities of defect sites can establish Zr⁴⁺/Zr-OH FLPs sites with improved activity and selectivity to unsaturated alcohols. The findings of this study indicate that the Zr⁴⁺/Zr-OH sites possess the ability to activate the C=O of aldehydes and -OH of cyclohexanol, resulting in a smaller activation energy barrier and exceptional catalytic performance. Additionally, it is noteworthy that the defective UiO-66 also demonstrates outstanding hydrogenation activity in the direct hydrogenation of α,β -unsaturated aldehydes, with a mere 6.8 KJ/mol activation energy required for the dissociation of H-H bonds. The possible reaction mechanism was proposed based on *in situ* DRIFT analysis. This work is valuable for the design and preparation of unsaturated aldehydes/ketones hydrogenation catalysts and provides a new idea for the design of solid FLPs catalysts.

1. Introduction

Catalytic Transfer Hydrogenation (CTH) using renewable liquid hydrogen-containing compounds (e.g. alcohols, acids, etc.) as the hydrogen source is regarded as an efficient and green reduction process [1,2]. Currently, most researchers only focus on the hydrogenation of substrate molecules, but ignore the dehydrogenation of hydrogen source compounds to produce value-added chemicals. However, the two-path reaction approach can significantly improve the economy of the process. As important chemical intermediates and fine chemical products, unsaturated alcohols can be obtained by the CTH of α,β -unsaturated aldehyde (Scheme 1) [3,4]. Acrolein (the simplest α,β -unsaturated aldehyde) has no functional group conjugated to the C=C bond and it is

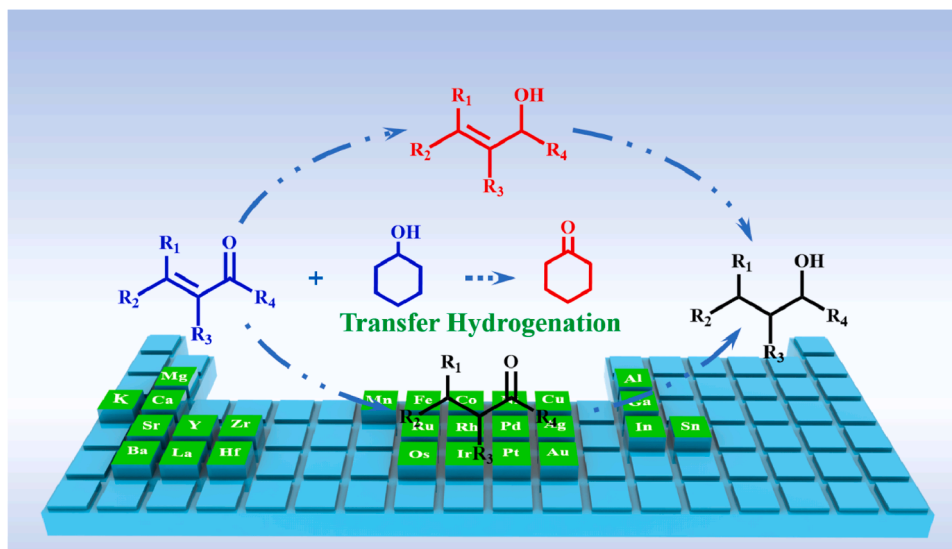
difficult to inhibit its reduction by weakening its adsorption stability due to site-blocking effects. Hence, the selective hydrogenation of acrolein to allyl alcohol is hard to achieve, and the key to solving this problem lies in the design and preparation of appropriate catalysts.

It is well known that the CTH is a typical Lewis acid/base cooperative catalytic reaction [2]. As shown in Fig. S1, Lewis acid sites can bond with the electron-rich oxygen in the -OH of the hydrogen donor and C=O of the hydrogen acceptor, while the adjacent Lewis base sites attract the hydrogen protons in the -OH group, thus forming a six-membered cyclic transition state to complete the CTH, commonly known as the Meerwein-Ponndorf-Velery (MPV) reaction. Unlike conventional Lewis acid-base reactions that form Lewis adducts, the solid Frustrated Lewis Pairs (FLPs) were developed in a variety of important

* Corresponding authors at: College of Chemical Engineering, Xiangtan University, Xiangtan 411105, China

E-mail addresses: lyyang@xtu.edu.cn (Y. Lv), liupingle@xtu.edu.cn (P. Liu).

¹ These authors contributed equally to this work and should be considered co-first authors.



Scheme 1. The route of the transfer hydrogenation of α,β -unsaturated aldehyde.

catalytic reactions including aldehyde hydrogenation, carbon dioxide reduction, and hydroamination [5–7]. Qu's group [5] constructed oxygen vacancy defects on the surface of cerium dioxide to create FLPs sites, which can easily dissociate H-H bonds with an activation energy of 0.17 eV. Ozin's group [8] prepared FLPs catalysts by attaching the surface hydroxyl group (OH) to the indium (In) surface and applied them in CO₂ reduction. These studies enable to construct FLPs catalysts by forming defects on the oxide surfaces, however, the design of highly active FLPs sites on the surface of inert metal oxide remains a significant challenge.

MOFs are widely used in catalysis, biomedicine, chemical sensors, adsorption, and hydrogen storage [9–11]. The constructed surface defects in MOF can facilitate the formation of unsaturated metal sites. UiO-66, with the general formula Zr₆O₄(OH)₄(BDC)₆, has been extensively studied due to its unique backbone structure that can accommodate a large number of defect sites [12]. The defects of UiO-66 are mainly caused by the absence of the linker (BDC), and the exposed defective vacancies can be compensated by modulators (monocarboxylic acids, hydroxides, methanol, fluorides, etc.). Therefore, catalysts with different active sites can be designed [13,14]. Currently, for unsaturated aldehyde CTH reactions, most defect MOFs are mainly considered as solid acid-base catalysts rather than FLPs catalysts [15, 16]. Moreover, there are few reports of direct construction of FLPs catalysts on the surface of UiO-66 [17–19].

In our previous study [20], we constructed the defect-rich ZIF-67 by microwave-assisted solvent method to form the FLPs catalyst with Co-N acid/base sites (Co-N distance 3.35 Å), presenting the activation energy of 8.7 Kcal/mol for the dissociation of H-H bond. Based on this, the metal-induced modifications of Zr-UiO-66 to form unsaturated zirconium sites and surface hydroxyl groups are investigated. Theoretically, the perfect Zr-UiO-66 does not provide the catalytic active site [21,22]. However, the defective UiO-66 tends to form unsaturated zirconium sites, and it is suggested that the unsaturated Zr site is the main source of Lewis acid [15,23,24].

Herein, the solid FLPs catalysts with rich -OH/Zr⁴⁺ active sites were constructed by monocarboxylic acid-induced defects formation in UiO-66 and applied in the transfer hydrogenation of α,β -unsaturated aldehydes using cyclohexanol as the hydrogen source. By providing hydrogen protons during transfer hydrogenation, cyclohexanol is dehydrogenated to cyclohexanone, an important intermediate for the production of adipic acid, caprolactam, and nylon. The results show that the formation of defect sites can construct Zr⁴⁺/Zr-OH FLPs sites with elevated activity and selectivity to unsaturated alcohols. Moreover, the

defective UiO-66 also exhibits excellent hydrogenation activity in direct hydrogenation of α,β -unsaturated aldehydes, and the possible reaction mechanism was proposed combined with *in situ* DRIFT. Meanwhile, the porous SiO₂-coated core-shell UiO-66 @SiO₂ catalyst exhibits high stability and excellent catalytic performance in the transfer hydrogenation of 15 different α,β -unsaturated aldehydes. This work will help to design and prepare unsaturated aldehydes/ketones selective hydrogenation catalysts.

2. Experimental

A complete description of chemicals, materials, characterization, and instrumentations is available in the [Supporting Information](#).

2.1. Synthesis of UiO-66

UiO-66 was synthesized by the solvothermal method [25]. See the [Supporting Information](#) for the detailed preparation process.

2.2. Synthesis of UiO-66-X

A certain amount of UiO-66 was placed into 55 mL of ultra-pure water, and different chain lengths of monocarboxylic acid regulator (0.6 mol/L of Formic Acid (FA), Acetic Acid (AA), Propionic Acid (PA)) was added, treated under ultrasonic for 10 min and transferred to a high-pressure reactor with 100 mL polytetrafluoroethylene lining. The reaction was performed at 70 °C for 4 h. After the reaction, the precipitate was collected by centrifugation (8000 rpm, 3 min), washed with water and ethanol for 2–3 times, and treated under reflux for 8 h, and dried in a vacuum to obtain the defective UiO-66-X (X represents H₂O, FA, AA, and PA, respectively).

2.3. Synthesis of UiO-66-FA@SiO₂

0.2 g of UiO-66-FA and a certain amount of CTAB were placed into a mixture of 60 mL of ethanol and 20 mL of ultra-pure water, ammonia was added to adjust the pH value to 8–9 under ultrasonic and then a certain amount of TEOS (5 drops/s) was added. After 4 h of reaction, the precipitate was collected by centrifugation (8000 rpm, 3 min). The precipitate was immersed in an ethanol solution for 2 days to remove CTAB and then dried in a vacuum at 60 °C to obtain UiO-66-FA@SiO₂.

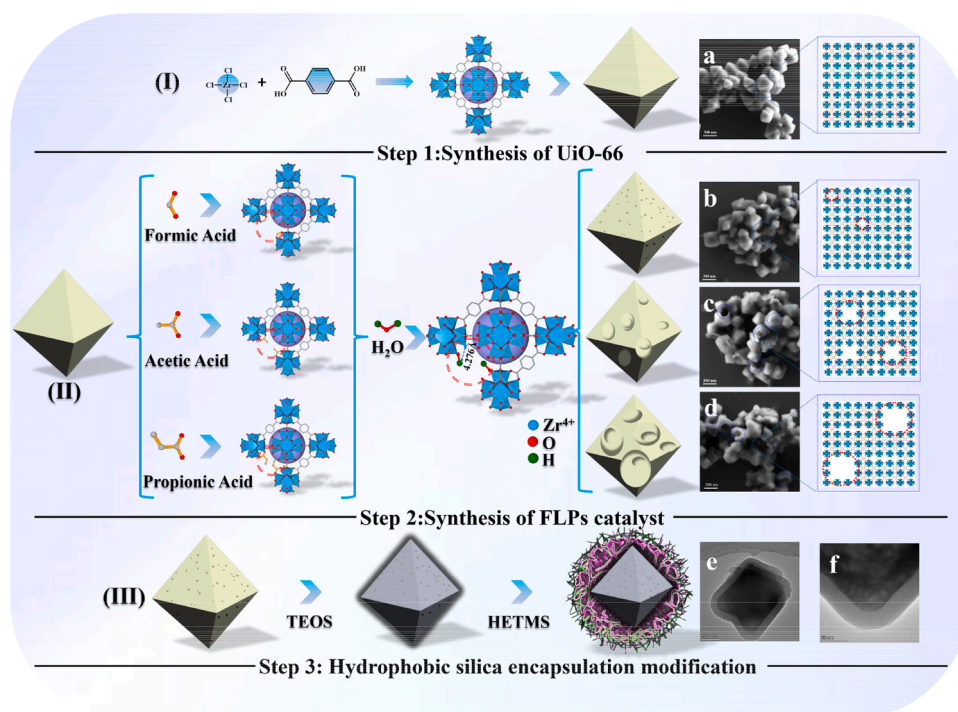


Fig. 1. Schematic diagram of the synthesis of solid FLPs catalysts; SEM images of UiO-66 (a), UiO-66-FA (b), UiO-66-AA (c), UiO-66-PA (d); TEM images of UiO-66-FA@SiO₂-HETMS (e, f).

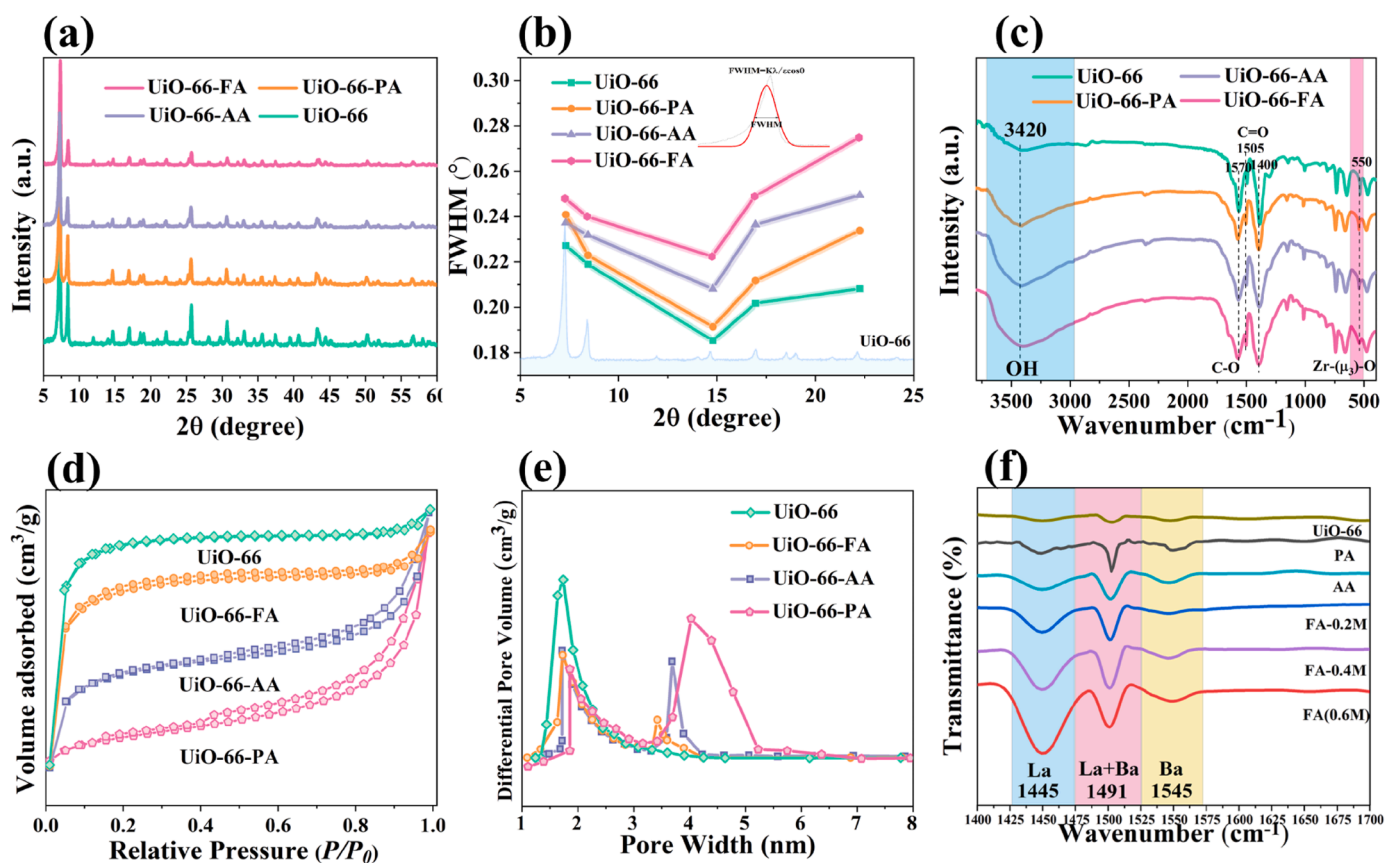


Fig. 2. PXRD (a), FWHM (b), FT-IR (c), N₂-physical adsorption and desorption curves (d), BJH pore size distribution (e), and Py-FITR (f) characterization of a series of UiO-66 samples.

Table 1

Textural Properties and Catalytic Activity of the Zr-MOFs for Acrolein hydrogenation and cyclohexanol dehydrogenation.

Enter	Catalyst	S_{BET} (m^2/g) ^a	A_M (m^2/g) ^b	D_p (nm) ^c	X_A (%)	S_a (%)	Y_a (%)	X_B (%)	Y_b (%)
1	Blank	/	/	/	< 1.2	/	/	/	/
2	UiO-66	1125	1044	1.96	32.67	72.45	30.06	40.4	40
3	UiO-66-H ₂ O	1129	1048	1.97	33.18	72.26	30.51	40.36	39.96
4	UiO-66-FA	982	908	2.79	100	71.1	71.1	97.3	96.33
5	UiO-66-AA	825	742	3.05	80.45	72.09	58	79.7	78.9
6	UiO-66-PA	608	365	3.68	64.82	71.13	39.04	51.74	51.22

^aSpecific surface area, ^bMicropore area, ^cAverage pore diameter; Reaction conditions: Acrolein, 0.5 g(8.74 mmol); Anol, 1 g (10 mmol), Catalyst, 50 mg; 5 g water; time, 11 h; temperature, 170 °C; Speed, 800 rpm; P_{N_2} , 1 MPa.

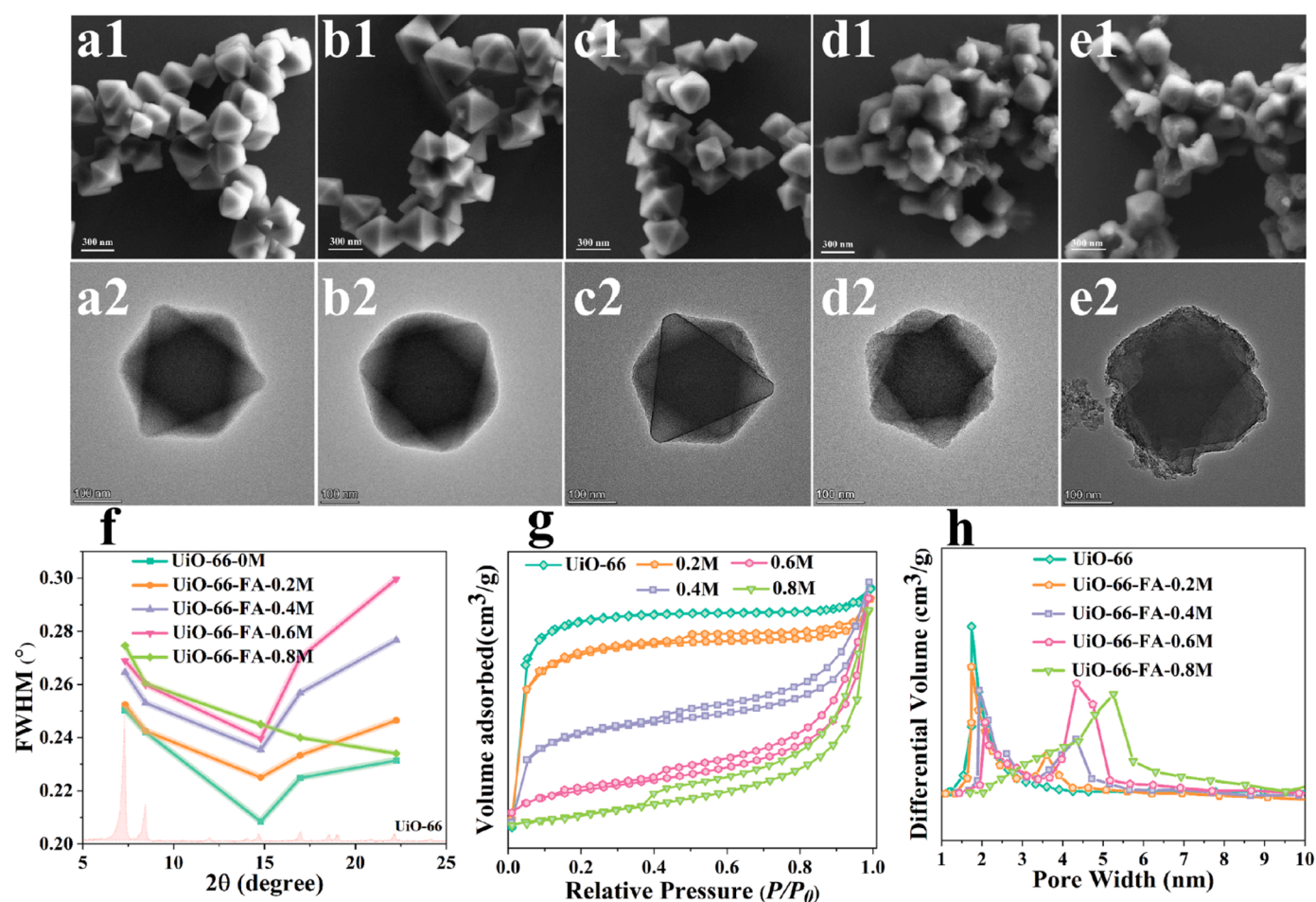


Fig. 3. SEM and TEM images of UiO-66 induced by different concentrations of formic acid (0 M (a1, a2), 0.2 M (b1, b2), 0.4 M (c1, c2), 0.6 M (d1, d2) and 0.8 M (e1, e2)) and characterization of half-peak widths (f), N₂-physical adsorption and desorption curves (g), BJH pore size distribution (h).

2.4. Synthesis of UiO-66-FA@SiO₂-HETMS

The detailed preparation process of the hydrophobic modified UiO-66-FA@SiO₂ (UiO-66-FA@SiO₂-HETMS) was shown in the [Supporting Information](#).

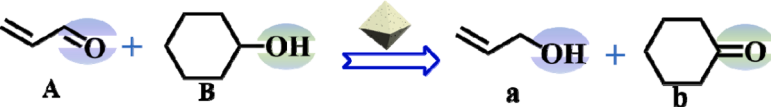
2.5. Catalytic tests

Catalytic transfer hydrogenation of α,β -unsaturated aldehydes to

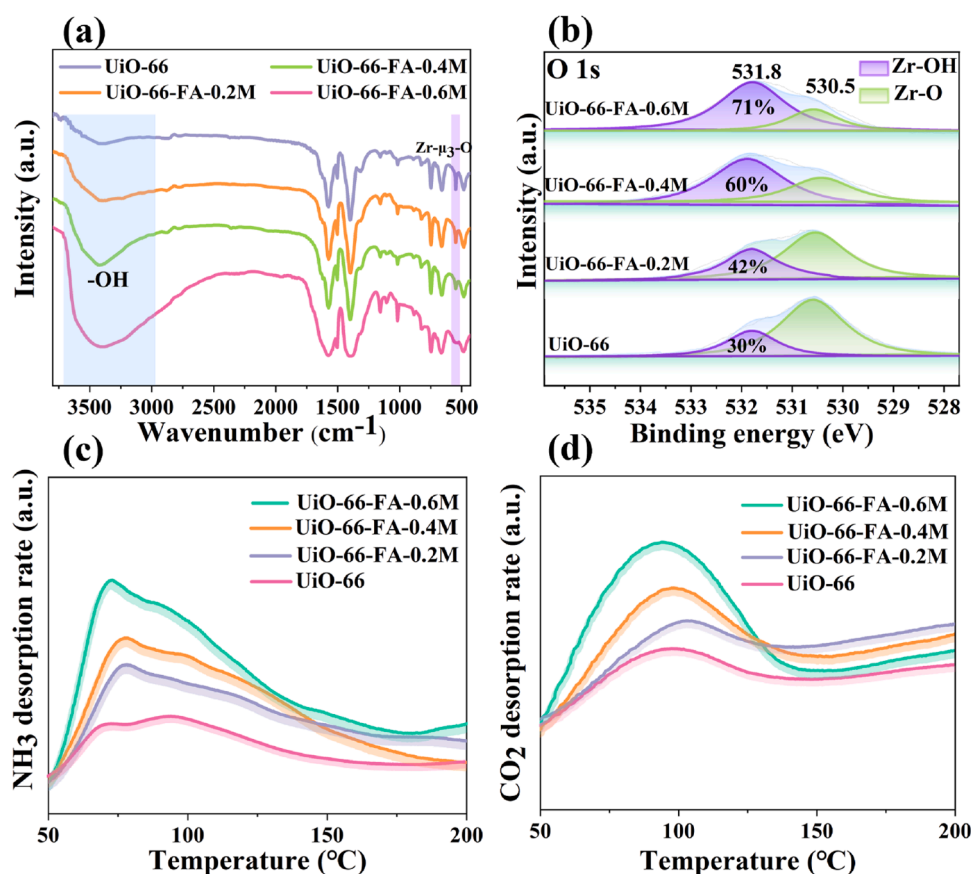
unsaturated alcohols in cyclohexanol was carried out in a high-pressure reactor. All catalysts were treated at 100 °C for 24 h prior to reacting. In a typical reaction, 50 mg of catalyst, 5 g of water, 9 mmol of α,β -unsaturated aldehyde, and slightly excessive cyclohexanol (10 mmol) were added to a 50 mL quartz liner. The reactor was sealed and purged with N₂ for 3 times, then filled with 1 MPa N₂. Subsequently, the reactor was heated to the required temperature and stirred at 800 r/min. After the reaction, the reactor was cooled to room temperature, and the reaction solution was extracted with 20 g ethyl acetate to separate

Table 2

Catalytic performance of the Zr-MOFs for acrolein hydrogenation and cyclohexanol dehydrogenation.



Enter	Catalyst	X _A (%)	S _a (%)	Y _a (%)	X _B (%)	Y _b (%)
1	UiO-66	32.67	72.45	30.06	40.4	40
2	UiO-66-FA-0.2 M	59.66	72.25	43.1	56.4	55.84
3	UiO-66-FA-0.4 M	83.54	71.81	60	79.65	78.85
4	UiO-66-FA-0.6 M	100	71.1	71.1	97.3	96.33
5	UiO-66-FA-0.8 M	34.52	71.32	24.62	31.31	31

Reaction conditions: Acrolein, 0.5 g (8.74 mmol); Anol, 1 g (10 mmol), Catalyst, 50 mg; 5 g water; time, 11 h; temperature, 170 °C; Speed, 800 rpm; P_{N2}, 1 MPa.**Fig. 4.** FT-IR (a), O1s XPS spectra (b), NH₃-TPD (c), and CO₂-TPD (d) of UiO-66, UiO-66-FA-0.2 M, UiO-66-FA-0.4 M, and UiO-66-FA-0.6 M.

the organic solvent from the water. The separated reaction solution was analyzed by Agilent 9720 A gas chromatograph (Agilent DB-1701) using n-butanol as the internal standard. To test the stability of the catalyst, the used catalyst was washed with ethanol for 3 times and dried in a vacuum at 60 °C for the next run. Correction factors and product analysis methods are shown in the [Supporting Information](#).

2.6. Theoretical calculations

Density Functional Theory (DFT) calculations were performed to simulate the possible defect sites of UiO-66 using UiO-66 single zirconium clusters as substrates and investigate the effect of the defects on the catalytic performance. Calculations were performed using the Perdew Burke-Ernzerhof (PBE) parameterized Generalized Gradient Approximation (GGA) methods. The Monkhorst-Pack k-point grid was set to

$2 \times 2 \times 2$ grid. The structural optimizations were performed using the self-consistent field (SCF) procedure, in which the convergence threshold was set to 10^{-5} au on the energy and electron density, all atoms were allowed to relax until the force was less than 0.02 eV/Å, and the convergence in energy, max force, and displacement was set to 2×10^{-5} Ha, 0.005 Ha/Å, and 0.005 Å, respectively. The adsorption energy (E_{ads}) was defined as: $E_{ads} = E_{adsorbate+surface} - E_{adsorbate} - E_{cleansurface}$. LST/QST was used to ensure that all transition states can be connected to the initial and final states, and with only one imaginary frequency.

3. Results and discussion

3.1. Design of UiO-66-based catalysts

[Fig. 1](#) illustrates the synthesis process of UiO-66, defective UiO-66,

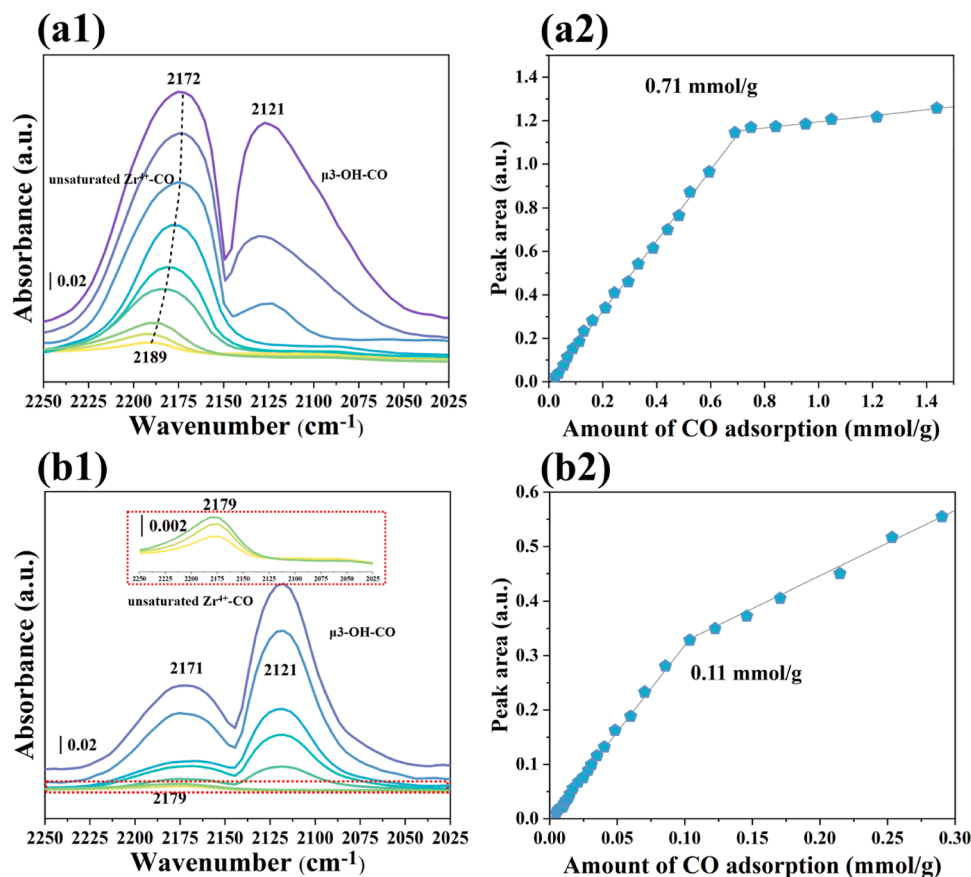


Fig. 5. CO-FTIR spectra of UiO-66-FA (a1) and UiO-66 (b1); Linear curves of CO adsorption versus unsaturated Zr^{4+} peak area for UiO-66-FA (a2) and UiO-66 (b2).

and hydrophobicity-modified SiO_2 -coated core-shell UiO-66 @ SiO_2 -HETMS. For UiO-66, $ZrCl_4$ and terephthalic acid were crystallized in DMF solution at 120 °C for 24 h to obtain perfect UiO-66 (Step 1). As to defective UiO-66, monocarboxylic acids (FA, AA, PA) are used to induce defect formation in UiO-66 by tailoring ligand vacancies. In detail, monocarboxylic acids compete with terephthalic acid and replace part of it so as to form the $-OH/Zr^{4+}$ FLPs sites (Step 2). SEM images in Fig. 1 (a-d) show that monocarboxylic acids with different lengths of carbon chain induce the formation of different amounts of defects in UiO-66. The reason may be that the different acidity coefficients of monocarboxylic acids affect their competitive adsorption with terephthalic acid and the defects of missing ligands [26,27]. Meanwhile, carbon chain length can affect the density and size of the defects. In addition, the possible structural formula of the defective UiO-66 was determined by dissolution/ 1H NMR spectra as $[Zr_{6-m}O_4(OH)_{4+n}(BDC)_{6-x}]$, the details are shown in Fig. S2 in the Supporting Information. For UiO-66 @ SiO_2 -HETMS, porous SiO_2 coating can effectively improve the stability of UiO-66, and hydrophobicity modification can regulate the adsorption and desorption of substrate and product on the catalyst surface (Step 3). As shown in Fig. 1(e-f), the SiO_2 coating on the surface of UiO-66 is about 25 nm thick.

3.2. Catalytic performance and characterization analysis

Fig. S3 shows the catalytic performance of different metal oxides in the transfer hydrogenation of acrolein. As shown in Fig. S3, the transition metal oxides (ZrO_2 , Co_3O_4 , NiO , and Fe_2O_3) show very poor hydrogenation activity. Similarly, other acidic oxides (Al_2O_3 , SiO_2) and basic oxides (ZnO , MgO) also exhibit low intrinsic activity. These results suggest that the metal oxides are inert in the catalytic transfer hydrogenation of acrolein to allyl alcohol.

Fig. 2(a) shows the PXRD patterns of UiO-66 induced by different monocarboxylic acids (FA, AA, and PA). It can be observed in Fig. 2(a) that the acid-induced UiO-66 possesses the same characteristic diffraction peaks as UiO-66 [25,28], indicating that the original crystalline structure is not destroyed after acid induction regulation. Moreover, the PXRD diffraction peaks of UiO-66-FA are more diffuse in comparison with UiO-66-AA and UiO-66-PA, indicating the weak crystallinity of UiO-66-FA [29]. Fig. 2(b) shows the PXRD-FWHM simulations of the samples, which can be used to characterize the surface defect concentration [30,31]. The positions of the diffraction peaks were chosen at 7.36°, 8.48°, 14.15°, 17.08°, and 25.68° and calculated using Gaussian fits (mean-adjacent method). According to the Scherrer equation, the FWHM is inversely proportional to the crystal size, and the crystal size is inversely proportional to the defect concentration, thus the FWHM is proportional to the defect concentration. As shown in Fig. 2(b), the FWHM of the samples present the following order: UiO-66-FA > UiO-66-AA > UiO-66-PA > UiO-66, indicating that UiO-66-FA contains the largest amounts of surface defects, which is conducive to the construction of more $Zr^{4+}/Zr-OH$ FLPs sites. Moreover, as seen in Fig. 2(d, e), the pore size of the samples gradually change from microporous to mesoporous with the addition of monocarboxylic acids, indicating that monocarboxylic acids induce the formation of defects. Raman spectrums of the samples are shown in Fig. S4. The two peaks near 1400 cm^{-1} correspond to the C-C and OCO vibration peaks of terephthalic acid, respectively. The characteristic peak at 836 cm^{-1} belongs to the C-C symmetric vibration peak of terephthalic acid, and the peak below 500 cm^{-1} ascribes to $Zr-(\mu_3)-O$ vibration [13,32,33]. It is noteworthy that the vibration peak intensity of C-C, OCO, and $Zr-(\mu_3)-O$ in UiO-66-FA is significantly weaker than that of other samples, indicating that more Zr ions in UiO-66-FA cannot coordinate with terephthalic acid, thus leading to more defects. In addition, Fig. S5 shows the TGA

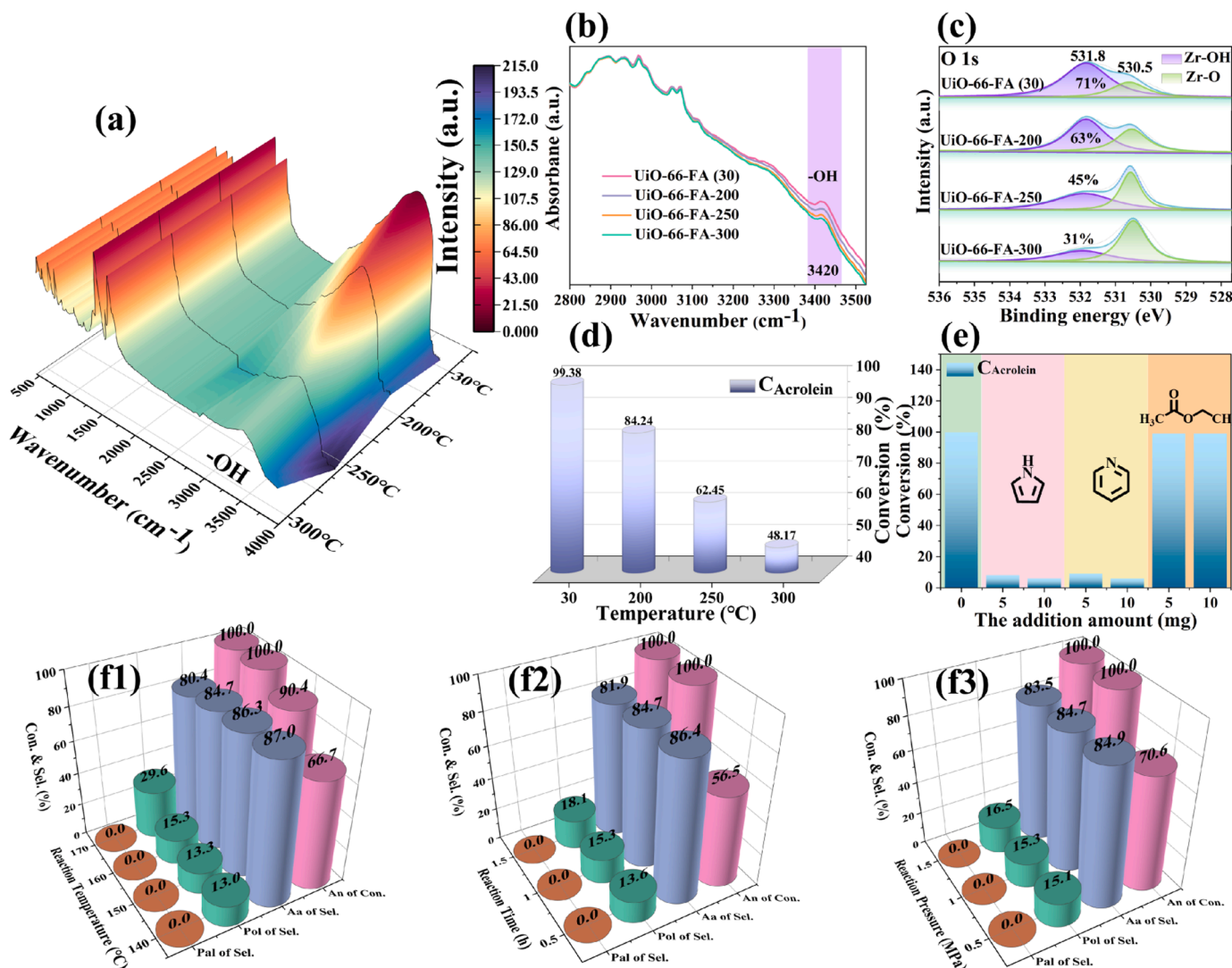


Fig. 6. Characterization of *in-situ* FT-IR (a), *vacuum* FT-IR (b), XPS (c), and catalytic performance of UiO-66-FA treated at different temperatures (d); Influences of Lewis acid sites or Lewis base sites of UiO-66-FA-0.6 M on the catalytic activity (e); Catalytic performance of UiO-66-FA-0.6 M in direct hydrogenation of acrolein under different reaction conditions (f1-f3).

characterization of the samples. There are four stages for the decomposition processes of the catalysts. The weight loss in the first stage (30–100 °C) ascribes to the adsorbed water. The second stage (100–320 °C) is due to the decomposition of Zr-OH, μ 3-OH, and monocarboxylic acid in UiO-66. It is worth noting that UiO-66-FA shows the largest weight loss at this stage (15% of weight loss), suggesting that the defect-rich UiO-66-FA lacks sufficient coordination between the ligand and the metal [34]. The third stage (320–580 °C) corresponds to the thermal decomposition of the organic skeleton of UiO-66 and the fourth stage (580–900 °C) attributes to the complete carbonization of the UiO-66. SEM images in Fig. 1(c, d) show that acid-induced UiO-66 exhibits abundant defects. Based on the results of PXRD, PXRD-FWHM, and TGA, it can be seen that UiO-66-FA has the largest amounts of defects.

FT-IR spectra of the samples are shown in Fig. 2(c). Before the test, the samples were treated at 100 °C for 24 h to exclude the physically adsorbed water (As shown in Fig. S6 in the Supporting Information, FTIR (near-infrared region) shows the absence of bound water (Zr-OH₂) in UiO-66-X). The characteristic peak that appears at 550 cm⁻¹ is attributed to Zr-(μ 3)-O vibration, indicating that the Zr ions coordinate with the μ 3-O bond in terephthalic acid [35,36]. Notably, the vibration peak intensity of Zr-(μ 3)-O in UiO-66-FA is significantly weaker than that of

other samples, indicating that more Zr ions in UiO-66-FA cannot coordinate with the μ 3-O bond, thus leading to more defects. Moreover, the characteristic peak at 3420 cm⁻¹ ascribes to the -OH vibration peak bound to Zr [37,38]. Interestingly, acid-induced UiO-66, especially the UiO-66-FA shows stronger peak intensity of surface hydroxyl groups than that of UiO-66, suggesting that the defects favor the formation of the hydroxyl groups. Additionally, Fig. 2(f) shows the Py-FTIR spectra of the samples. As seen in Fig. 2(f), the peak at 1445 cm⁻¹ belongs to Lewis acids derived from the Zr⁴⁺ sites [15,22,39] and its intensity increases obviously after the acid induction. The results demonstrate that acid induction facilitates the formation of defects as well as exposes more unsaturated Zr⁴⁺ sites. It is widely accepted that the surface hydroxyl groups are generally considered as the Lewis bases [8,15,40]. Therefore, the Zr-OH sites (Lewis base) and the adjacent unsaturated Zr⁴⁺ sites (Lewis acid) on the defective UiO-66 may construct the solid Frustrated Lewis Pairs (FLPs) sites.

Table 1 summarizes the texture properties of UiO-66-based catalysts and their catalytic performance in the transfer hydrogenation of acrolein in cyclohexanol. It was found that no products (allyl alcohol and cyclohexanone) are obtained in the absence of the catalysts (Table 1, Entry 1). As shown in Entries 2 and 3, water-treated UiO-66-H₂O has almost the same textural properties and catalytic performance as UiO-

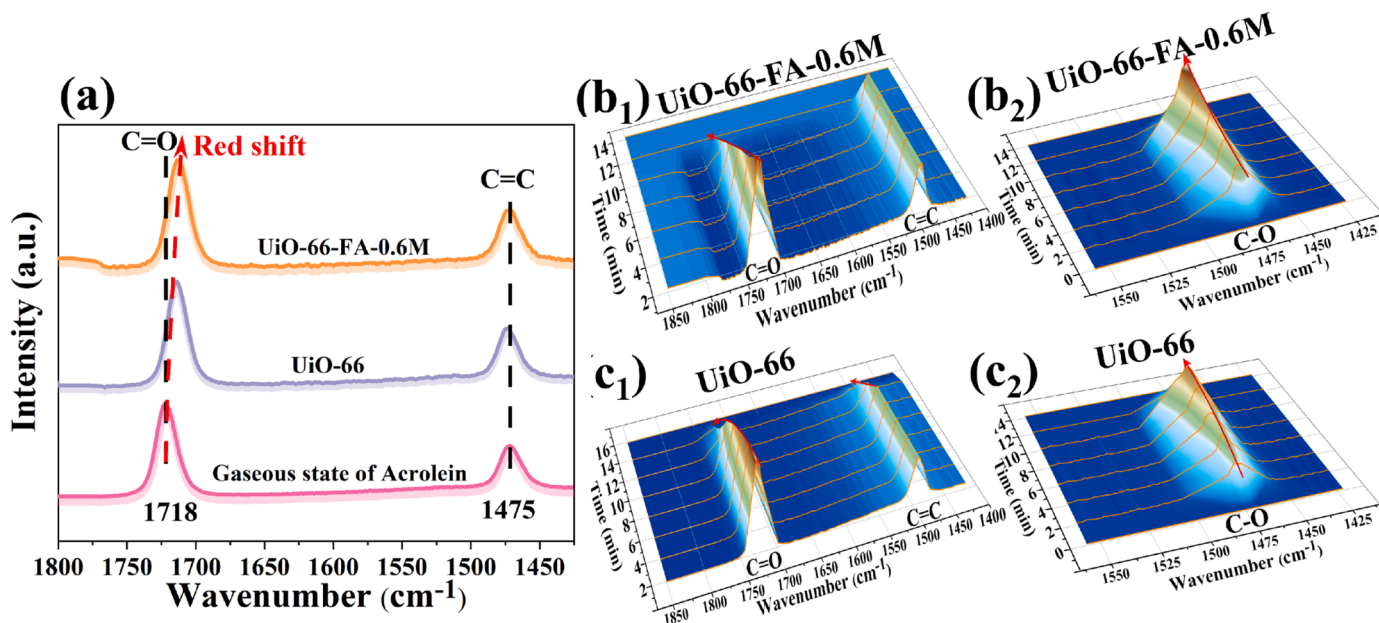


Fig. 7. The *In-situ* DRIFTS spectra of absorbed acrolein on the UiO-66-FA-0.6 M and UiO-66 (a); *In-situ* DRIFTS spectra of the acrolein hydrogenation over UiO-66-FA-0.6 M (b₁, b₂) and UiO-66 (c₁, c₂).

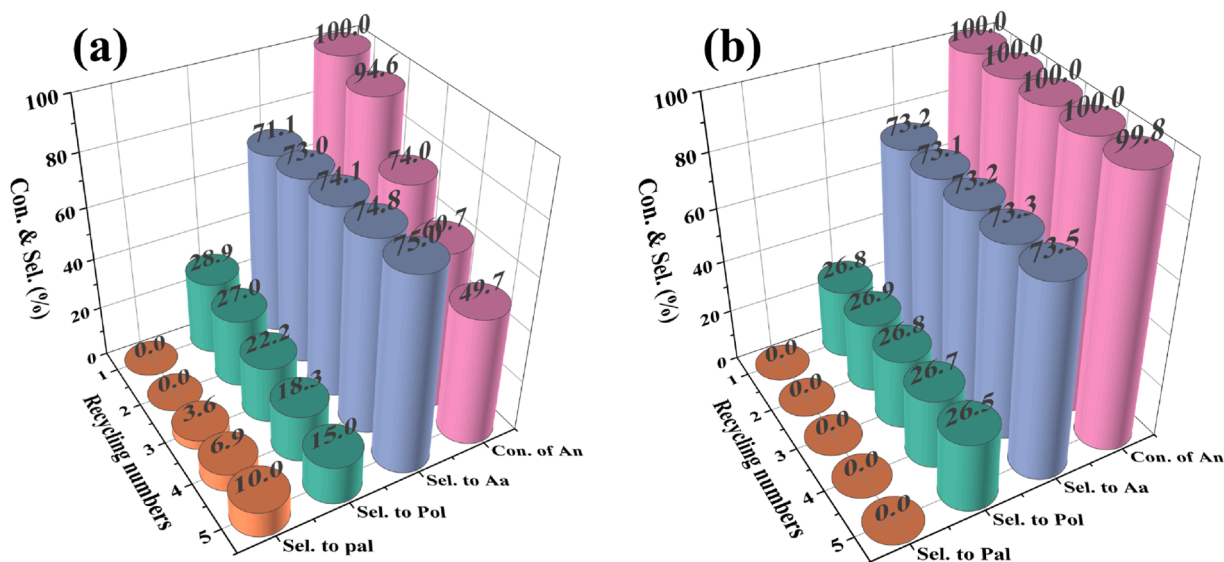


Fig. 8. Catalytic stability of the UiO-66-FA-0.6 M (a) and UiO-66-FA@SiO₂ (b). Reaction conditions: Acrolein, 0.5 g (8.74 mmol); Anol, 1 g (10 mmol), Catalyst, 50 mg; 5 g water; time, 11 h; temperature, 170 °C; Speed, 800 rpm; P_{N₂}, 1 MPa.

66, indicating that water does not affect the modulation. Moreover, Entries 4–6 show that the specific surface area and micropore area decrease obviously with the introduction of monocarboxylic acids, the reason may be that monocarboxylic acids induce massive terephthalic acid shedding, thereby exposing the abundant sites of Zr⁴⁺/Zr-OH FLPs sites. It should be noted that the acrolein conversion over UiO-66-FA is more than three times higher than that of the UiO-66 (Entries 2 and 4). The ICP results in Table S1 confirm that the UiO-66-FA possesses the highest Zr⁴⁺ content. Moreover, the Zr⁴⁺ active sites are generally encapsulated by the ligand, whereas monocarboxylic acids induction can expose more Zr⁴⁺/Zr-OH FLPs sites. Meanwhile, the catalytic activity of UiO-66-AA and UiO-66-PA is lower than UiO-66-FA, the reason may be the shedding of a large amount of Zr clusters, which can be inferred from the pore size and ICP data in Table S1.

The effects of the concentration of the monocarboxylic acids on the

surface defects of UiO-66-FA are investigated. Fig. 3(a1-e2) show the SEM and TEM images of UiO-66-FA with different concentrations (0.2 M, 0.4 M, 0.6 M, and 0.8 M). It can be seen the surface roughness of the UiO-66-FA gradually increases with the increase of formic acid concentration from 0.2 M to 0.8 M, especially when the concentration is up to 0.8 M, UiO-66-FA begins to disintegrate, indicating that the excess formic acid can cause the whole Zr clusters to fall out of the UiO-66 framework. CO-TPD is used to characterize the densities of defects on the catalyst surface [34,41]. As shown in Fig. S7, UiO-66-FA (0.6 M) presents the strongest CO desorption peak, indicating the highest densities of defects. XRD-FWHM in Fig. 3(f) and Raman spectrums in Fig. S8 further confirm this. Moreover, as seen in Fig. 2(f), Py-FTIR spectra of the UiO-66-FA (0.6 M) exhibit the strongest peak intensity of Lewis acid, indicating that UiO-66-FA (0.6 M) has the largest amount of exposed unsaturated Zr⁴⁺ sites. Unfortunately, as shown in Fig. 3(f, g, h), the

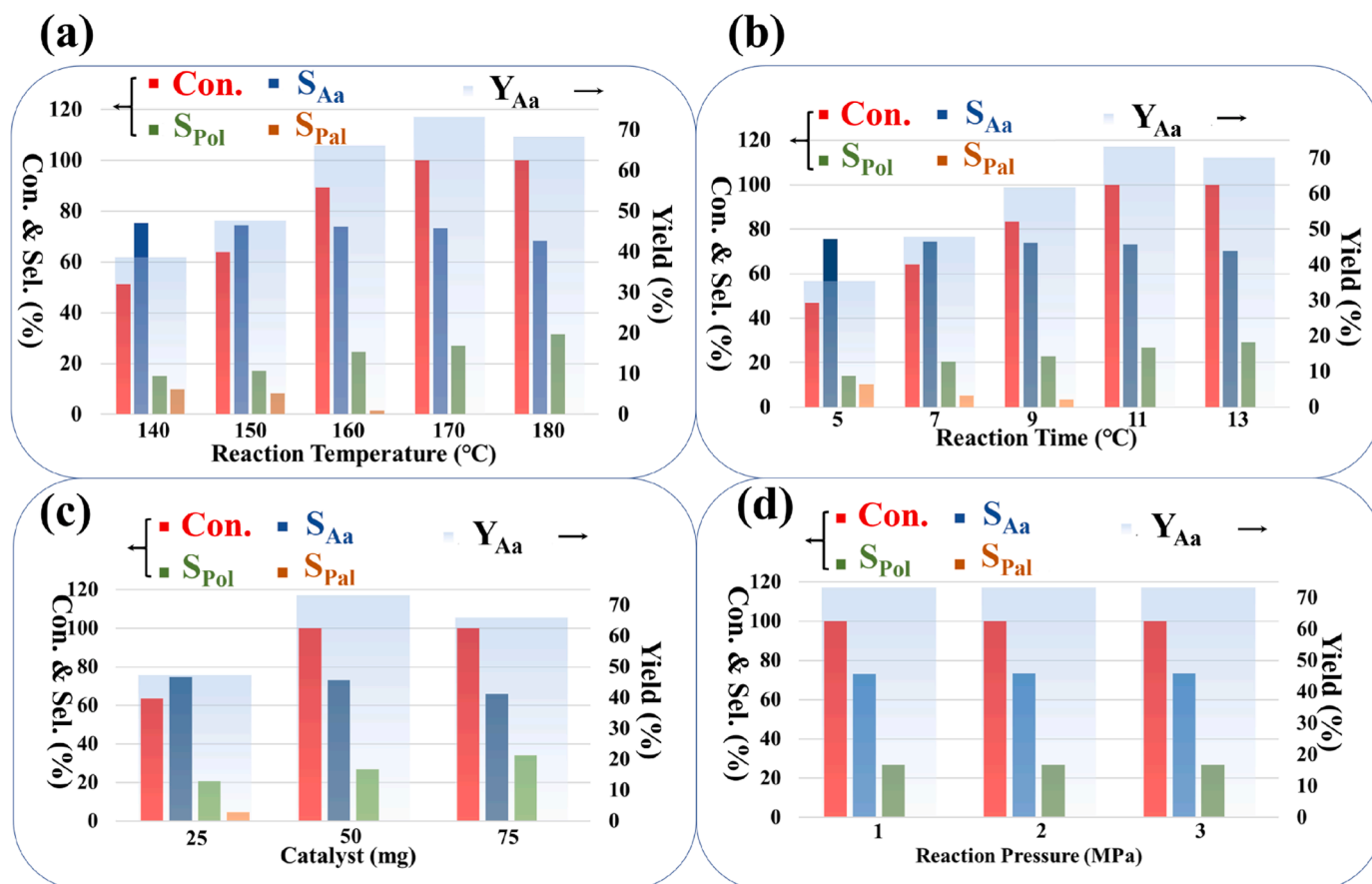


Fig. 9. Catalytic performance of UiO-66-FA@SiO₂ under different reaction conditions (Acrolein, CTH). Identical reaction conditions: acrolein, 0.5 g (8.74 mmol); cyclohexanol, 1 g (10 mmol); 5 g water; Speed, 800 rpm. Different reaction conditions: Catalyst, 50 mg; time, 11 h; P_{N₂}, 1 MPa (a); Catalyst, 50 mg; temperature, 170 °C; P_{N₂}, 1 MPa (b); time, 11 h; temperature, 170 °C; P_{N₂}, 1 MPa (c); Catalyst, 50 mg; time, 11 h; temperature, 170 °C (d).

structure of UiO-66-FA-0.8 M collapses with too higher FA concentration. The SEM image in Fig. S9 also confirms this. Thus, UiO-66-FA-0.8 M presents poor catalytic activity in the transfer hydrogenation of acrolein in Table 2.

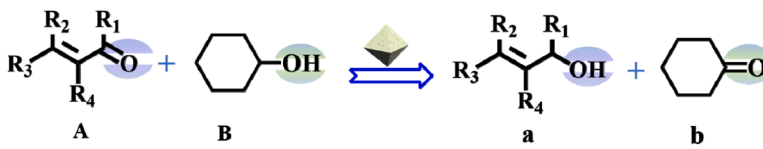
3.3. Identification of the role of -OH/Zr⁴⁺

The UiO-66-FA prepared with different concentrations of FA were treated at 100 °C for 24 h to eliminate the effect of physically adsorbed water. FT-IR spectra in Fig. 4(a) show that UiO-66-FA-0.6 M possesses the largest amount of unsaturated Zr ions, incoordinate with the μ 3-O bond in terephthalic acid, resulting in more defects. Also, it is noteworthy that UiO-66-FA-0.6 M presents the strongest characteristic peak intensity of the -OH vibration at 3420 cm⁻¹, indicating that the largest amount of surface hydroxyl groups is formed. Furthermore, the O1s XPS in Fig. 4(b) further confirms that the UiO-66-FA-0.6 M contains the highest peak area occupancy (71%) of Zr-OH (531.8 cm⁻¹) [42,43]. As can be seen in Fig. S10, the states of Zr in the UiO-66 are all ortho-tetravalent [43,44]. The results of NH₃-TPD in Fig. 4(c) show that the acidic intensity of the UiO-66-FA tends to increase with the increase of FA concentration, and UiO-66-FA-0.6 M exhibits the strongest peak intensity of NH₃ desorption, further indicating that it has the largest amount of exposed unsaturated Zr⁴⁺ sites. This is consistent with the result of Py-FTIR in Fig. 2(f).

As shown in Fig. 5, the absolute number of unsaturated zirconium sites in UiO-66-FA-0.6 M was further quantified. Fig. 5 (a1) shows the CO-FTIR spectrum of UiO-66-FA. At the initial stage of CO adsorption, the characteristic peak of ν (CO) appears at 2189 cm⁻¹. With the increase of CO adsorption, ν (CO) peak shows a significant red-shift, indicating

that unsaturated Zr⁴⁺ bonds with CO to form unsaturated zirconium carbonyl compounds. When the unsaturated zirconium is saturated with the adsorbed CO, an additional peak of ν (CO) appears at 2121 cm⁻¹, which is attributed to both μ 3-OH-CO and physically adsorbed CO [15, 45]. As shown in Fig. 5(a2, b2), the amount of unsaturated Zr⁴⁺ in UiO-66 and UiO-66-FA is quantified by the linear relationship curves of CO adsorption versus unsaturated Zr⁴⁺ peak area. Compared with chemical adsorption, the physical adsorption of CO has relatively weak interaction forces, so the linear relationship curve weakens when the chemisorbed amount (unsaturated Zr⁴⁺-CO) reaches saturation [15,46]. The adsorption of CO by UiO-66-FA starts to slow down at 0.71 mmol/g, indicating that the unsaturated Zr⁴⁺ adsorption reaches saturation, which means that UiO-66-FA contains 0.71 mmol/g of unsaturated Zr⁴⁺ defect sites. However, UiO-66 possesses only 0.11 mmol/g of unsaturated Zr⁴⁺ defect sites. Meanwhile, the results of CO₂-TPD in Fig. 4(d) show that the UiO-66-FA-0.6 M possesses the strongest peak intensity of CO₂ desorption, suggesting that it has the highest basic intensity, derived from the surface hydroxyl groups. Thus, it can be seen that the largest amount of Zr⁴⁺/Zr-OH active sites exist in UiO-66-FA-0.6 M. Meanwhile, the results in Table 2 indicate that the conversion of acrolein and cyclohexanol increases with the increment of the content of Zr⁴⁺/Zr-OH sites in UiO-66-FA. Therefore, Zr⁴⁺/Zr-OH sites play an important role in the catalytic transfer hydrogenation.

To further explore the role of Zr⁴⁺/Zr-OH in the transfer hydrogenation of acrolein, the catalytic performances of UiO-66-FA with different Zr-OH contents were investigated and shown in Fig. 6. TGA results in Fig. S5 show that the cleavage of Zr⁴⁺/Zr-OH is around 300 °C. Thus, UiO-66-FA-0.6 M was treated at different temperatures (200 °C, 250 °C, and 300 °C) under a nitrogen atmosphere to obtain UiO-66-FA

Table 3Catalytic performance of the UiO-66-FA@SiO₂ for substrate expansion (CTH).


Entry	Substrate	Main product	X _A (%)	S _a (%)	Y _b (%)	CLogP ^a	Time (h)
1			> 99	81.42	98.4	0.296	11
2			> 99	88.69	> 99	0.52	11
3			> 99	92.73	99.1	0.919	12
4			> 99	90.41	> 99	1.049	10
5			98.54	95.3	97.2	1.358	11
6			99.04	95.05	96.9	1.578	11
7			> 99	> 99	> 99	0.671	12
8			> 99	94.61	> 99	-0.367	12
9			95.57	96.06	94.5	1.225	12
10 10 ^b			> 91.84 > 99	93.67 93.5	91.4 > 99	2.049	12
11 11 ^b			90.44 > 99	96.23 96.84	89.4 98.2	2.358	13
12 12 ^b			90.05 > 99	96.71 97.26	89.4 96.4	2.792	13 11
13 13 ^b			92.39 > 99	97.27 96.38	90.2 97.5	2.652	13 11
14 14 ^b			92.71 98.54	93.33 94.45	90.4 97.5	2.192	13 12
15 15 ^b			91.22 99.4	93.95 93.59	89.3 95.4	2.548	13 12

Reaction conditions: Substrate, 0.5 g (8.74 mmol); Cyclohexanol, 1 g (10 mmol), Catalyst, 50 mg; 5 g water; time, 11 h; temperature, 170 °C; Speed, 800 rpm; P_{N₂}, 1 MPa; ^a cLogP of reaction substrate calculated using ChemDraw 19.0; ^b Using a hydrophobic UiO-66-FA@SiO₂-HETMS.

with different Zr-OH contents. The *in-situ* FT-IR and *vacuum* FT-IR spectra in Fig. 6(a, b) show that the peak intensity of the -OH vibration (3420 cm⁻¹) gradually decreases with the increase of treatment temperature. Similarly, O1s XPS in Fig. 6(c) indicates that the peak area of the -OH decreases from 71% to 30% as the treatment temperature increases from 30 °C to 300 °C. Correspondingly, the results in Fig. 6(d) show that the conversion of acrolein significantly decreases from 99.38% to 48.17%. It is known that the addition of free Lewis acid and Lewis base molecules during the reaction can verify the Lewis acid/base sites in the FLPs catalysts. The pyrrole as Lewis acid can be directly adsorbed on the basic site, and similarly, the pyridine as Lewis basic can

be adsorbed on the acidic sites, i.e., they can efficiently close the FLPs sites [5,8,47]. As shown in Fig. 6(e), the addition of pyrrole or pyridine completely inhibits the catalytic activity, while the addition of the neutral substance (ethyl acetate) basically keeps the catalytic activity unchanged. These results demonstrate the necessity for the coexistence of acid-base Lewis sites in Zr⁴⁺/Zr-OH FLPs catalysts. Meanwhile, the GC-MS results showed that H₂ was the main source of hydrogen rather than liquid hydrogen-containing compounds in direct hydrogenation, the details are shown in Fig. S11 in the Supporting Information. Undoubtedly, FLPs catalysts possess an excellent ability to adsorb and dissociate H₂ [5–7]. Herein, the direct hydrogenation of acrolein in the

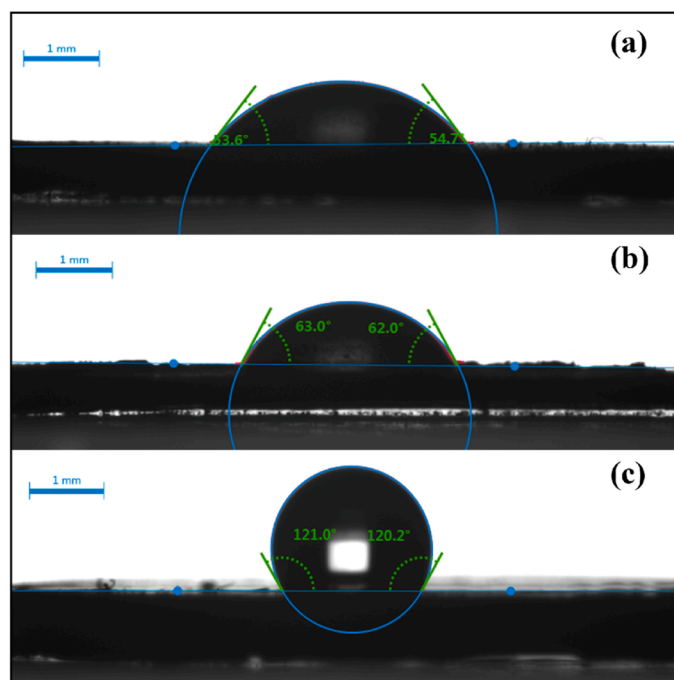


Fig. 10. Static Water Contact Angle Analysis of UiO-66-FA (a), UiO-66-FA@SiO₂ (b), and UiO-66-FA@SiO₂-HETMS (c).

H₂ system over UiO-66-FA-0.6 M was investigated. As expected in Fig. 6 (f1-f3), UiO-66-FA-0.6 M gives a very good catalytic performance of 100% conversion of acrolein and 84.7% selectivity to allyl alcohol.

3.4. Study on the adsorption, activation, and desorption processes of acrolein

In-situ DRIFTS were carried out to study the adsorption, activation, and desorption of acrolein and the hydrogenation process. Fig. 7(a) shows the *In-situ* DRIFTS spectra of the adsorbed acrolein on the surface of UiO-66 and UiO-66-FA-0.6 M. Two forms of orbital peaks appear at 1718 cm⁻¹ and 1475 cm⁻¹, attributing to $\nu(\text{C}=\text{O})$ and $\nu(\text{C}=\text{C})$ in acrolein, respectively [48]. Compared with gaseous acrolein, the UiO-66 and UiO-66-FA-0.6 M show significant redshifts to the $\nu(\text{C}=\text{O})$ orbit. Noticeably, UiO-66-FA-0.6 M presents the largest redshift, indicating that it preferentially adsorbs and activates C=O rather than C=C.

In-situ DRIFTS spectra of acrolein hydrogenation over UiO-66-FA-0.6 and UiO-66 are shown in Fig. 7(b1, b2) and (Fig. 7(c1, c2)), respectively. As the reaction proceeds, the orbital peak intensity of the C=O is gradually weakening, while the C=C remains essentially unchanged (Fig. 7(b1, c1)). As shown in Fig. 7(b2, c2), the orbital peak of C-O in the alcohol appears at 1089 cm⁻¹ [49], indicating that the activated hydrogen (H*) derived from H₂ dissociation preferentially adsorbs on the C=O bond and then forms the C-O bond. More importantly, the C=O orbital peak in Fig. 7(b1) decreases faster than that in Fig. 7(c1), suggesting that allyl alcohol is easier to form on UiO-66-FA-0.6 M. Typically, the *in-situ* hydrogenation of acrolein lasted only 10 min, then the *in-situ* cell was purged with argon flow to make the allyl alcohol desorb. As shown in Fig. 7(b2, c2), it takes two minutes for allyl alcohol desorption from UiO-66-FA-0.6 M, but four minutes for UiO-66, indicating that allyl alcohol is easier to desorb from UiO-66-FA-0.6 M, thus preventing its further hydrogenation.

3.5. Recycle of the catalysts

Fig. 8(a) shows the recycle stability of UiO-66-FA-0.6 M. It can be seen that the conversion over UiO-66-FA-0.6 M decreases from 100% to

49.7% for the fifth run, indicating that the recycle stability is poor. As can be seen from the PXRD and TEM images in Fig. S13(a), after the first cycle, the PXRD diffraction peak of UiO-66-FA-0.6 M starts to become diffuse. Meanwhile, a broad and large characteristic diffraction peak of amorphous ZrO₂ appears at 28° [50,51]. This indicates that part of the skeleton of UiO-66-FA-0.6 M is severely disrupted. After the fifth cycle, the skeleton of UiO-66-FA-0.6 M is completely collapsed and transformed into amorphous ZrO₂. As shown in Fig. S12, thermal filtration experiments and kinetic studies are performed to verify whether the filtrate and ZrO₂ derived from the dissolution of UiO-66-FA-0.6 M participates in the hydrogenation reaction. The experimental results show that the uncollapsed UiO-66-FA-0.6 M is the “real catalyst” and not the filtrate or amorphous ZrO₂ (For a detailed discussion, see Supporting Information Fig. S12). The porous silica shell was tried to coat on the catalyst surface to improve the recycle stability [52–55]. Detailed methods are described in the Supporting Information. The PXRD pattern of UiO-66-FA@SiO₂ is shown in Fig. S13(b). The characteristic peaks of UiO-66-FA are still present in UiO-66-FA@SiO₂, indicating that the silica coating does not affect the original crystalline structure. Meanwhile, a broad and weak characteristic peak appears at 23°, belonging to the amorphous SiO₂ [56,57], indicating that the SiO₂ successfully covers the UiO-66-FA surface. Furthermore, according to the TEM and Mapping in Figs. S13(c) and S14(a), it can be visualized that SiO₂ is successfully encapsulated on the surface of UiO-66-FA and the elements are uniformly dispersed. The N₂-physical adsorption and desorption curves and the BJH pore size distribution indicate that the silica coating does not affect the accessibility of the substrate molecules to the active centers, the details are shown in Fig. S15 in the Supporting Information. The results in Fig. 8(b) show that the stability of UiO-66-FA@SiO₂ remains essentially unchanged after the fifth cycle. The PXRD in Fig. S13(b) and TEM images in Fig. S14(b) show that the characteristic PXRD diffraction peaks and morphology of the fifth recycled UiO-66-FA@SiO₂ remain almost unchanged. Furthermore, ICP results in Table S3 further confirm that the Zr content of the fifth recycled UiO-66-FA@SiO₂ (27.6%) is almost the same as the fresh UiO-66-FA@SiO₂ (27.7%).

3.6. Catalytic performance of UiO-66-FA@SiO₂

The catalytic performances of UiO-66-FA@SiO₂ under different reaction conditions are shown in Figs. 9 and S16. Fig. 9(a) shows that the conversion of acrolein gradually increases as the temperature increases, while the selectivity to allyl alcohol decreases when the temperature reaches 180 °C, indicating that acrolein is mainly over-hydrogenated to n-propanol. Moreover, it can be seen from Fig. 9(b) that the acrolein is completely converted till 11 h and the selectivity to allyl alcohol begins to decrease as the reaction time continues to extend. In addition, Fig. 9 (c) and (d) show that the optimal catalyst dosage is 0.05 g and the N₂ pressure has no effect on the performance. Under optimum conditions, UiO-66-FA@SiO₂ gives 73.2% selectivity to allyl alcohol at 100% acrolein conversion, and the yield to cyclohexanone reaches 96.3%. Meanwhile, the GC-MS results show that no etherification products are detected in all reactions, as shown in Fig. S17. It indicates that acrolein does not undergo etherification under this catalytic system.

Table 3 summarizes the catalytic performance of the UiO-66-FA@SiO₂ for 15 common α,β -unsaturated aldehydes. Compared with acrolein (Entry 1), 2-methylacrolein is more difficult to convert, but it shows higher selectivity to unsaturated alcohol. It may be because the presence of a methyl group on the α -C increases the steric hindrance on the C=C bond, making the C=C bond difficult to be adsorbed, thus improving the selectivity to unsaturated alcohol. Meanwhile, similar results can be found in Entry 2 and Entry 3, Entry 4 and Entry 5, and Entry 10 and Entry 11. As shown in Entries 1–8, the corresponding conversion of α,β -unsaturated aldehydes are greater than 98%. The effects of the hydrophilic and hydrophobic properties of the catalyst surface on the catalytic performance should be considered. ClogP can be used to represent the hydrophobic and hydrophilic properties, and the

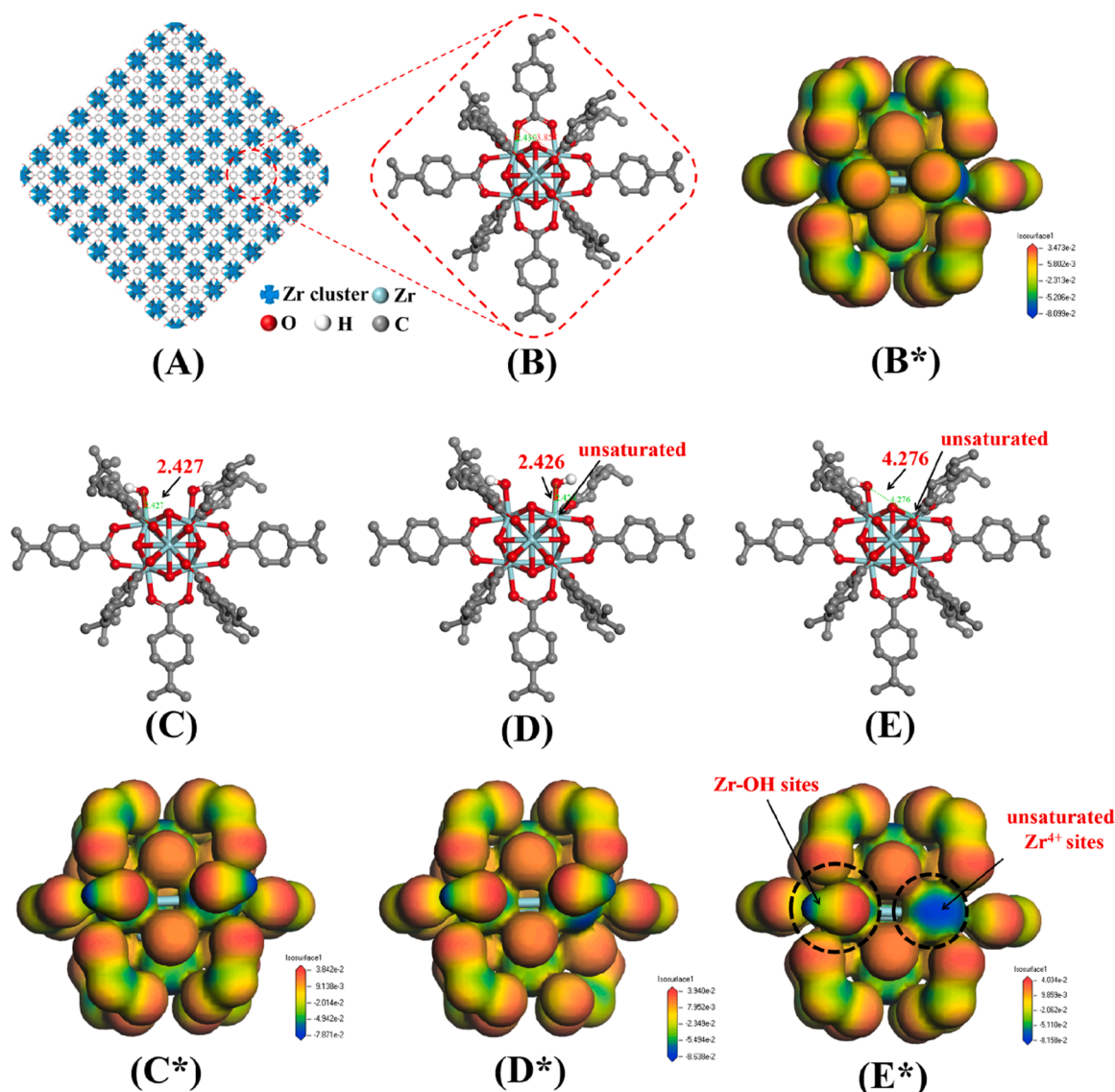


Fig. 11. The comparison of the perfect and defect UiO-66. UiO-66's Basic Metal-Organic Framework (A), perfect UiO-66 node (B), defect UiO-66 node (Zr-OH (C), Zr⁴⁺-OH (D), Zr⁴⁺/Zr-OH (E), Zr is the saturated state; Zr⁴⁺ is the unsaturated state); The electron-density isosurface of the B*~E* structures.

larger the ClogP value, the stronger the hydrophobic of the compound. Herein, as seen in Entries 10–15, these unsaturated aldehydes with strong hydrophobicity do not show better results. Notably, it can be seen from Entries 10^b–15^b that the hydrophobic modified UiO-66-FA@SiO₂ (UiO-66-FA@SiO₂-HETMS) presents a higher catalytic performance in the hydrogenation of α,β -unsaturated aldehydes. The conversions are greater than 98%, and the yields to cyclohexanone are greater than 95%. The PXRD of Fig. S13(d) shows that SiO₂-HETMS is successfully encapsulated on UiO-66-FA. Meanwhile, the static water contact angle characterizations in Fig. 10 shows that the contact angles of UiO-66-FA and UiO-66-FA@SiO₂ are 53.6° and 62.0°, respectively, while the contact angle of UiO-66-FA@SiO₂-HETMS reaches 121.0°, indicating the strong hydrophobicity of UiO-66-FA@SiO₂-HETMS. Furthermore, Table S4 summarizes the catalytic performances of UiO-66-FA@SiO₂ in direct hydrogenation of α,β -unsaturated aldehydes. Noticeably, owing to the efficient activation of H₂ by Zr⁴⁺/Zr-OH FLPs sites in UiO-66-FA, UiO-66-FA@SiO₂ can achieve the efficient conversion of unsaturated aldehydes in a short time of 1–1.5 h. Additionally, compared with the reported results in Table S5, UiO-66-FA@SiO₂ exhibits promising applications in the selective hydrogenation of α,β -unsaturated aldehydes.

3.7. DFT calculations

Fig. 11 shows the perfect UiO-66 node (B), defective UiO-66 node (Zr-OH (C), Zr⁴⁺-OH (D), and Zr⁴⁺/Zr-OH (E)) modeled by fabricating defective sites on the UiO-66. It should be noted that the Lewis base (Zr-OH) site is not present in the B, C, and D structures and does not meet the conditions for the formation of FLPs sites. However, for the structure E, the open unsaturated Zr⁴⁺ site and the adjacent Zr-OH site act as Lewis acid and Lewis base, respectively, with a distance of 4.276 Å, satisfying the conditions for the formation of FLPs sites. Also, the electron density isosurface of the B*~E* structures are shown in Fig. 11. Notably, as can be seen in Fig. 11(E*), the Zr-OH site in the E* structure has more abundant electrons, while the unsaturated Zr⁴⁺ site exhibits the greatest electron scarcity, which may suggest that the Zr⁴⁺/Zr-OH FLPs site is more likely to be the active center for the dissociated hydrogen source.

Fig. S18 shows the adsorption model of the acrolein on the B~E structures at the parallel, perpendicular, and top positions of the zirconium cluster. Moreover, Fig. S19 shows the calculated results of acrolein adsorption energy, and Table S6 summarizes the calculated results of the adsorption model and the C_a=O_a bond distance of acrolein. As can be seen from Fig. S19 and Table S6, acrolein prefers to adsorb in the vertical

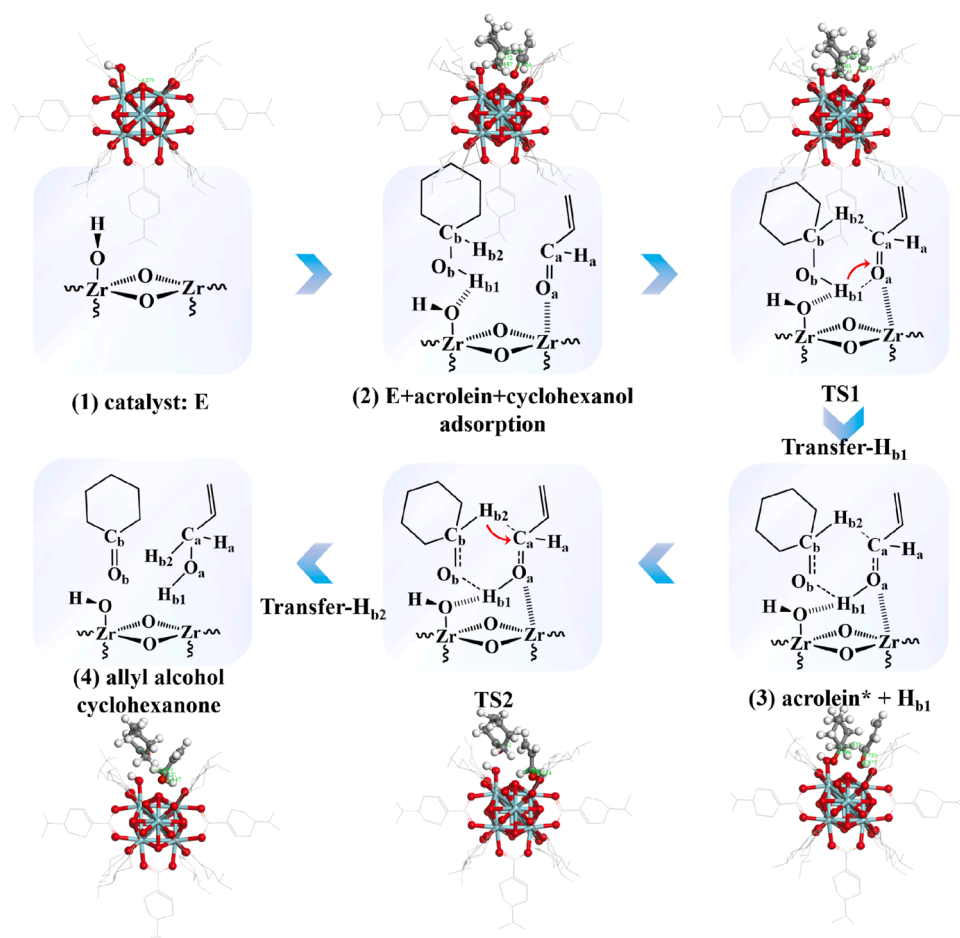


Fig. 12. Optimized structures with bond distance (in Å) for acrolein transfer hydrogenation to allyl alcohol and cyclohexanol dehydrogenation to cyclohexanone on the E structure.

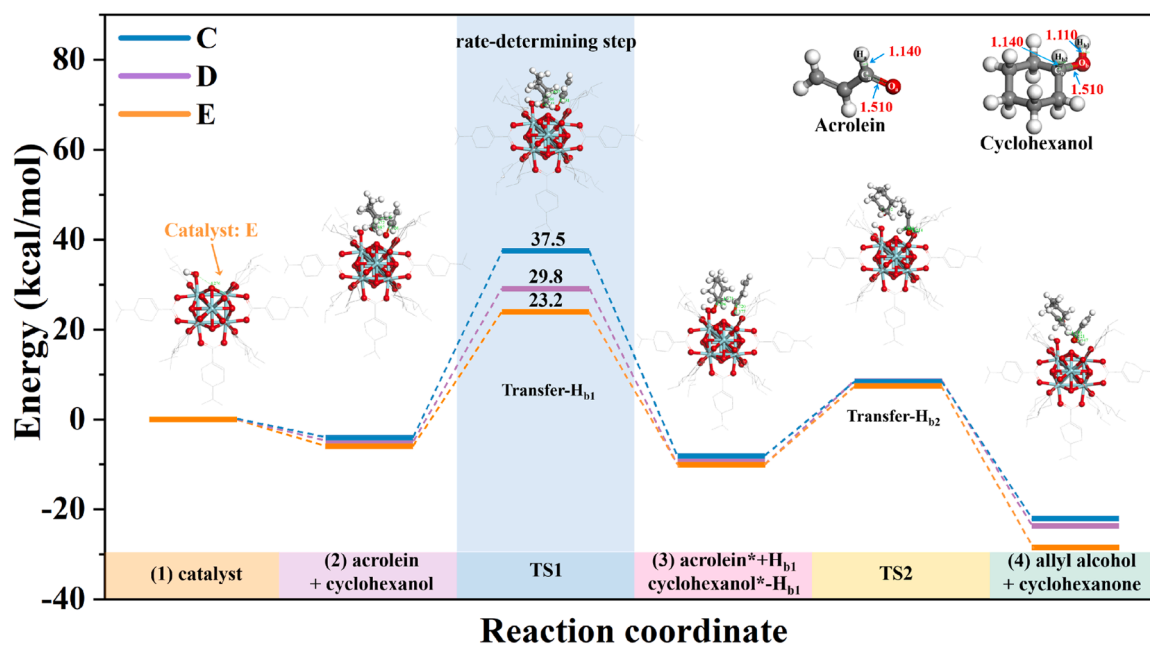


Fig. 13. Calculated energy profiles for the potential comparative free energy of acrolein transfer hydrogenation to allyl alcohol and cyclohexanol dehydrogenation to cyclohexanone on the C, D, and E structures.

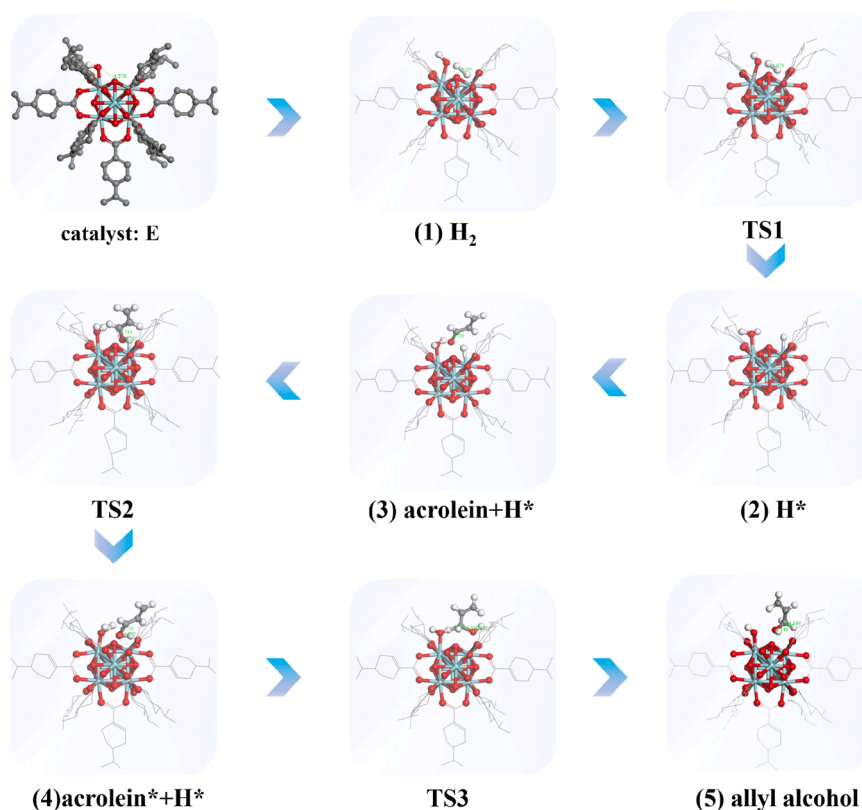


Fig. 14. Optimized structures with bond distance (in Å) for acrolein direct hydrogenation to allyl alcohol on the E structures.

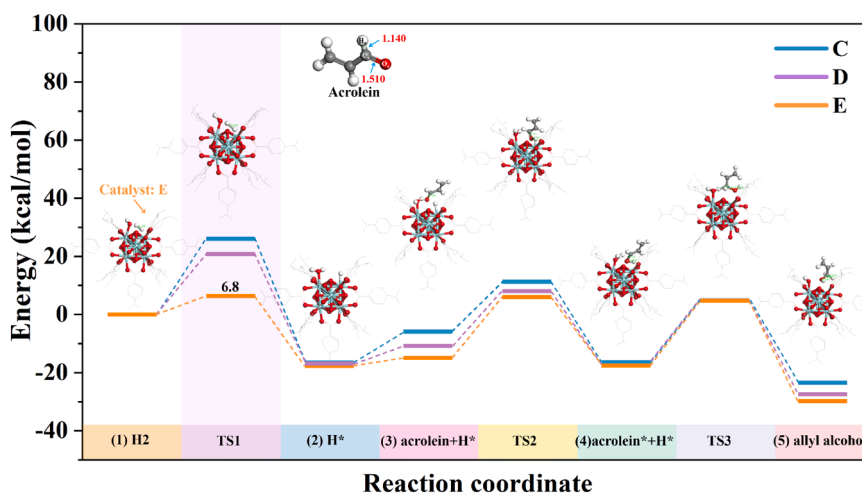


Fig. 15. Calculated energy profiles for the potential comparative free energy of acrolein direct hydrogenation to allyl alcohol on the C, D, and E structures.

state after the optimization of the computational model. The largest acrolein adsorption energy on the B~E structures are -0.09 eV, -2.77 eV, -3.78 eV, and -3.95 eV, respectively. Meanwhile, the $C_a=O_a$ bonds of acrolein are stretched to 1.515 Å, 1.611 Å, 1.703 Å, and 1.726 Å, respectively. The results show that the E structure presents the largest adsorption energy of acrolein, and the $C_a=O_a$ is stretched to 1.726 Å, indicating that acrolein is more easily adsorbed and activated on the E structure. Afterward, Fig. S20 shows the adsorption model of cyclohexanol on the B~E structures, and the calculated results are shown in Fig. S21, and the bond distances of C_b-O_b and O_b-H_{b1} in cyclohexanol are summarized in Table S7. As shown in Fig. S20 and Table S7, the E structure exhibits the largest adsorption energy of cyclohexanol (-3.93 eV), and the distances of the C_b-O_b and O_b-H_{b1}

bond are stretched to 1.672 Å and 1.387 Å, respectively, suggesting that the E structure can effectively promote the cyclohexanol molecule adsorption and activation. On the contrary, the largest adsorption energies of acrolein and cyclohexanol on the B structure are -0.09 eV and -0.08 eV, respectively, it can be considered that they cannot be adsorbed and activated. Thus, the B structure is no longer discussed below. Furthermore, the adsorption model of allyl alcohol on the B~E structures and the calculated results are shown in Figs. S22 and S23, respectively, and Table S8 summarizes the bond distances of C_a-O_a in allyl alcohol. As shown in Fig. S23 and Table S8, the E structure presents the lowest adsorption energy of -2.04 eV and the smallest C_a-O_a bond distance of 1.521 Å, indicating that allyl alcohol is easier to desorb from the E structure.

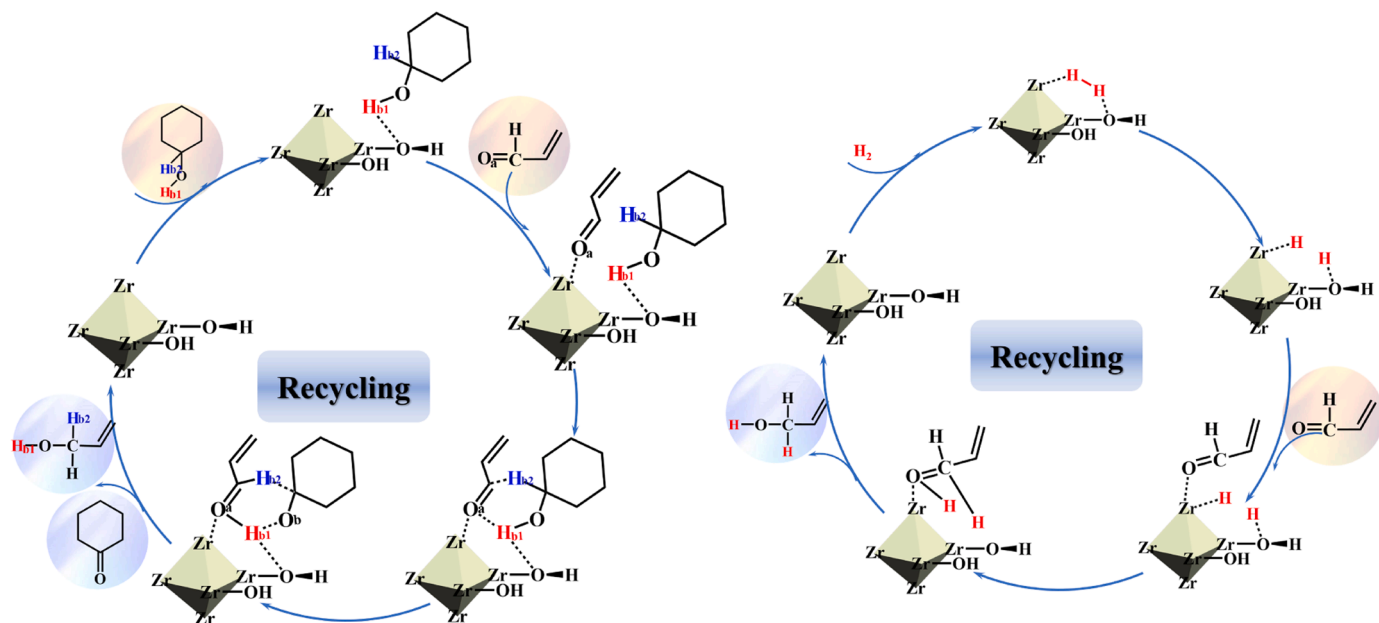


Fig. 16. Proposed mechanism for acrolein transfer hydrogenation (a) and direct hydrogenation(b) to allyl alcohol on the $\text{Zr}^{4+}/\text{Zr-OH}$ FLP sites.

Furthermore, Fig. S24 shows the adsorption model of cyclohexanone on the B~E structures. Likewise, Fig. S25 and Table S9 show that the E structure exhibits the lowest adsorption energy of -1.84 eV and the smallest $\text{C}_b=\text{O}_b$ bond distance of 1.515 Å, indicating that cyclohexanone is easier to desorb from the E structure.

The optimized structures of the intermediates and transition states with bond distances (in Å) for acrolein transfer hydrogenation to allyl alcohol and cyclohexanol dehydrogenation to cyclohexanone on the E structure are shown in Fig. 12 and Table S10. As shown in Fig. 12, the transfer hydrogenation reaction is a typical six-membered ring transition state reaction. Moreover, the optimized structures and bond lengths of the transition states for this reaction on the C, D, and E structures are depicted in Figs. S20-S27 and Table S10. The calculated energy profiles for the potential comparative free energy of the transfer hydrogenation of acrolein to allyl alcohol and the dehydrogenation of cyclohexanol to cyclohexanone on the C~E structures are shown in Fig. 13. The energy barrier changes for the whole reaction of the C~E structures are summarized in Table S15. As can be seen from Figs. 12 and 13, the H_{b1} of cyclohexanol preferentially adsorbs on the O atom of Zr-OH , and O_a of acrolein preferentially adsorbs on the Zr^{4+} site. In TS1, the O_b-H_{b1} bond and $\text{C}_a=\text{O}_a$ bond are preferentially stretched to 1.326 Å and 1.605 Å, respectively, indicating that the O_b-H_{b1} bond and $\text{C}_a=\text{O}_a$ bond are activated. Subsequently, the H_{b1} in the O_b-H_{b1} bond is preferentially transferred to the $\text{C}_a=\text{O}_a$ bond. Moreover, the energy barriers of the TS1 on the C~E structures are 71.3 Kcal/mol, 60.9 Kcal/mol, 57.1 Kcal/mol, 37.5 Kcal/mol, 29.8 Kcal/mol, and 23.2 Kcal/mol, respectively, indicating that the O_b-H_{b1} bond and $\text{C}_a=\text{O}_a$ are easier to be activated on the E structure. In TS2, the C_b-H_{b2} bond in cyclohexanol is stretched to 1.321 Å, and then the H_{b2} transfers to the C_a atom of acrolein, resulting in the formation of allyl alcohol and cyclohexanone. In this case, the energy barriers of the TS2 on the C~E structures are 12.4 Kcal/mol, 11.9 Kcal/mol, 11.9 Kcal/mol, 9.2 Kcal/mol, 8.7 Kcal/mol, and 7.5 Kcal/mol, respectively. The results indicate that the energy barrier of TS1 is much higher than TS2, therefore TS1 is the rate-determining step of the whole reaction. Moreover, the energy barrier of TS1 on the E structure is relatively small, further revealing that $\text{Zr}^{4+}/\text{Zr-OH}$ FLPs sites can effectively activate the $\text{C}=\text{O}$ of aldehydes and $-\text{OH}$ of cyclohexanol, thus exhibiting excellent catalytic performance.

Fig. S28 shows the adsorption model of H_2 on the B~E structures. Fig. S29 and Table S12 summarize the calculated results of the

adsorption model and the distance of the H-H bond. As shown in Fig. S29 and Table S12, the E structure presents the largest adsorption energy of H_2 (-3.98 eV), and the H-H bond is stretched to 1.978 Å, indicating that H_2 on easier to adsorb and dissociate into active H^* . After that, Fig. S30 shows the adsorption model of H^* on the B~E structures, and the calculated results are summarized in Fig. S31 and Table S13. It can be seen that the E structure presents the lowest adsorption energy of H^* (-0.72 eV), indicating that H^* is easier to desorb from the E structure.

The optimized structure and bond lengths for the transition state of the direct hydrogenation of acrolein to allyl alcohol on the E structure are shown in Fig. 14 and Table S14. The calculated energy profiles for the potential comparative free energy of the direct hydrogenation of acrolein to allyl alcohol on the C~E structure are shown in Fig. 15 and Table S15. In TS1, the energy barriers for the dissociation of H_2 on the C~E structures are 79.6 Kcal/mol, 77.5 Kcal/mol, 76.2 Kcal/mol, 26.4 Kcal/mol, 20.3 Kcal/mol, and 6.8 Kcal/mol, respectively. It is noteworthy that the energy barriers of TS1 on the E structure are relatively small, indicating that the E structure can efficiently absorb and dissociate H_2 . In TS2, the $\text{C}_a=\text{O}_a$ bond is activated by stretching, and H^* preferentially attacks O_a to form the C_a-O_a bond. Similarly, the E structure presents the lowest energy barrier of TS2 (6.1 Kcal/mol). In TS3, another H^* adsorbs on the C_a of the C_a-O_a bond to form allyl alcohol. Noticeably, the E structure exhibits the lowest energy barrier in the whole reaction, further indicating that the constructed $\text{Zr}^{4+}/\text{Zr-OH}$ FLPs sites can effectively activate H_2 and promote the hydrogenation of acrolein to allyl alcohol. Thus, it can be seen that the above DFT calculations are in good agreement with the experimental results.

Fig. 16 shows the possible reaction mechanism of the transfer hydrogenation (a) and the direct hydrogenation (b) of acrolein on the $\text{Zr}^{4+}/\text{Zr-OH}$ FLP sites. In transfer hydrogenation, the O_a atom on acrolein adsorbs on the Zr^{4+} site and the H_{b1} atom in cyclohexanol adsorbs on the Zr-OH site. In detail, the H_{b1} of cyclohexanol is preferentially transferred to the O_a of acrolein to form the $\text{C}-\text{O}_a$ bond, then the H_{b2} of cyclohexanol is transferred to the $\alpha\text{-C}$ of acrolein to form the allyl alcohol and cyclohexanone. Briefly, H^* is directly transferred from alcohols via the six-membered ring transition state to the carbonyl group. The CTH reaction in this study falls within the realm of MPV reaction mechanisms. Meanwhile, similar results were reported in previous studies of the CTH reaction [58,59]. In direct hydrogenation, the H_2 molecules are activated and dissociated into H^* on the $\text{Zr}^{4+}/\text{Zr-OH}$ FLP

sites, and the two H^{*} are adsorbed on the Lewis acid (Zr⁴⁺) site and Lewis base (Zr-OH) site, respectively. After that, the C=O of acrolein is activated by the Zr⁴⁺ site, and the H^{*} reacts with the activated C=O to form allyl alcohol.

4. Conclusion

In summary, a series of defective UiO-66 were prepared using different monocarboxylic acids and applied in the selective hydrogenation α,β -unsaturated aldehydes to unsaturated alcohols in the cyclohexanol system. It was found that the constructed surface defect in UiO-66 promotes the emergence of Zr-OH sites (Lewis base) and the neighboring unsaturated Zr⁴⁺ sites (Lewis acid) on the surface of UiO-66-FA, thereby generating solid Frustrated Lewis Pairs (FLPs) sites. Furthermore, the manipulation of the densities of defect sites can establish Zr⁴⁺/Zr-OH FLPs sites with improved activity and selectivity to unsaturated alcohols. The findings of this study indicate that the Zr⁴⁺/Zr-OH sites possess the ability to activate the C=O of aldehydes and -OH of cyclohexanol, resulting in a smaller activation energy barrier and exceptional catalytic performance. Additionally, it is noteworthy that the defective UiO-66 also demonstrates outstanding hydrogenation activity in the direct hydrogenation of α,β -unsaturated aldehydes, with a mere 6.8 KJ/mol activation energy required for the dissociation of H-H bonds. The possible reaction mechanism was proposed based on *in situ* DRIFT analysis. Also, the recycle stability of the UiO-66-FA was significantly enhanced by coating porous SiO₂. Substrate extension experiments show that this work is valuable for the design and preparation of unsaturated aldehydes/ketones hydrogenation catalysts and provides a new idea for the design of solid FLPs catalysts.

CRediT authorship contribution statement

Linhao Zhong: Methodology, Software, Validation, Investigation, Writing – original draft, Formal analysis, Data curation, Visualization. **Xiaoqing Liao:** Software, Validation, Investigation, Writing – original draft, Formal analysis, Data curation, Visualization. **Haishuai Cui:** Software, DFT calculations, Investigation, Validation. **Hean Luo:** Resources, Supervision, Project administration. **Yang Lv:** Conceptualization, Methodology, Software, Data curation, Writing – review & editing, Investigation, Supervision, Resources, Visualization, Funding acquisition. **Pingle Liu:** Resources, Supervision, Writing – review & editing, Project administration, Formal analysis, Funding acquisition.

Declaration of Competing Interest

The authors declare that they have no known competing financial interests or personal relationships that could have appeared to influence the work reported in this paper.

Data availability

Data will be made available on request.

Acknowledgments

This work was supported by NSFC (22078277), Hunan Provincial Natural Science Foundation of China (2023JJ30577), the Scientific Research Fund of Hunan Provincial Education Department (21C0078), Collaborative Innovation Center of New Chemical Technologies for Environmental Benignity and Efficient Resource Utilization, Environment-friendly Chemical Process Integration Technology Hunan Province Key Laboratory, and Postgraduate Scientific Research Innovation Project of Hunan Province (XDCX2023Y187).

Appendix A. Supporting information

Experimental section; reported catalytic systems for the selective hydrogenation of α,β -Unsaturated aldehydes; reaction mechanism of CTH; additional characterization (N₂ adsorption-desorption isotherms, CO₂-TPD, NH₃-TPD, CO-TPD, SEM, Raman spectra, XPS, XRD, TEM, EDX-Mapping, *In-situ* DRIFTS spectra, Dissolution/¹H NMR, GC-MS); adsorption models and calculations results of acrolein, allyl alcohol, cyclohexanol, cyclohexanone, H₂ and H^{*} on A~E structures; The bond lengths of reactants and calculation of product transition states (TS) on A~E structures.

Appendix A. Supporting information

Supplementary data associated with this article can be found in the online version at doi:10.1016/j.apcatb.2023.123421.

References

- [1] Y. Ren, Y. Yang, L. Chen, L. Wang, Y. Shi, P. Yin, W. Wang, M. Shao, X. Zhang, M. Wei, Synergetic effect of Cu⁰-Cu⁺ derived from layered double hydroxides toward catalytic transfer hydrogenation reaction, *Appl. Catal. B Environ.* 314 (2022), 121515, <https://doi.org/10.1016/j.apcatb.2022.121515>.
- [2] S. Zhou, F. Dai, Z. Xiang, T. Song, D. Liu, F. Lu, H. Qi, Zirconium-lignosulfonate polyphenolic polymer for highly efficient hydrogen transfer of biomass-derived oxygenates under mild conditions, *Appl. Catal. B Environ.* 248 (2019) 31–43, <https://doi.org/10.1016/j.apcatb.2019.02.011>.
- [3] L. Zhang, M. Zhou, A. Wang, T. Zhang, Selective hydrogenation over supported metal catalysts: from nanoparticles to single atoms, *Chem. Rev.* 120 (2020) 683–733, <https://doi.org/10.1021/acs.chemrev.9b00230>.
- [4] M. Zhao, K. Yuan, Y. Wang, G. Li, J. Guo, L. Gu, W. Hu, H. Zhao, Z. Tang, Metal-organic frameworks as selectivity regulators for hydrogenation reactions, *Nature* 539 (2016) 76–80, <https://doi.org/10.1038/nature19763>.
- [5] S. Zhang, Z.Q. Huang, Y. Ma, W. Gao, J. Li, F. Cao, L. Li, C.R. Chang, Y. Qu, Solid frustrated-Lewis-pair catalysts constructed by regulations on surface defects of porous nanorods of CeO₂, *Nat. Commun.* 8 (2017), <https://doi.org/10.1038/ncomms15266>.
- [6] Z. Wan, C. Wang, C. Yang, D. Ma, H. Ji, C. Chen, W. Ma, J. Zhao, Unusual catalytic hydrogenation caused by photoinduced solid frustrated Lewis pairs, *Appl. Catal. B Environ.* 324 (2023), 122237, <https://doi.org/10.1016/j.apcatb.2022.122237>.
- [7] S. Wang, Y. Xia, G. Yan, M. Chen, X. Wang, L. Wu, R. Liang, PDI bridged MIL-125 (Ti)-NH₂ heterojunction with frustrated Lewis pairs: A promising photocatalyst for Cr(VI) reduction and antibacterial application, *Appl. Catal. B Environ.* 317 (2022), 121798, <https://doi.org/10.1016/j.apcatb.2022.121798>.
- [8] K.K. Ghuman, L.B. Hoch, P. Szymanski, J.Y.Y. Loh, N.P. Kherani, M.A. El-Sayed, G. A. Ozin, C.V. Singh, Photoexcited surface frustrated Lewis pairs for heterogeneous photocatalytic CO₂ reduction, *J. Am. Chem. Soc.* 138 (2016) 1206–1214, <https://doi.org/10.1021/jacs.5b10179>.
- [9] H. Furukawa, K.E. Cordova, M. O’Keeffe, O.M. Yaghi, The chemistry and applications of metal-organic frameworks, *Science* 341 (2013), <https://doi.org/10.1126/science.1230444>.
- [10] Q. Yang, D. Gao, C. Li, S. Wang, X. Hu, G. Zheng, G. Chen, Highly dispersed Pt on partial deligandation of Ce-MOFs for furfural selective hydrogenation, *Appl. Catal. B Environ.* 328 (2023), 122458, <https://doi.org/10.1016/j.apcatb.2023.122458>.
- [11] N. Stock, S. Biswas, Synthesis of metal-organic frameworks (MOFs): Routes to various MOF topologies, morphologies, and composites, *Chem. Rev.* 112 (2012) 933–969, <https://doi.org/10.1021/cr200304e>.
- [12] D. Yang, V. Bernalles, T. Islamoglu, O.K. Farha, J.T. Hupp, C.J. Cramer, L. Gagliardi, B.C. Gates, Tuning the surface chemistry of metal organic framework nodes: proton topology of the metal-oxide-like Zr₆ nodes of UiO-66 and NU-1000, *J. Am. Chem. Soc.* 138 (2016) 15189–15196, <https://doi.org/10.1021/jacs.6b08273>.
- [13] X. Feng, H.S. Jena, C. Krishnaraj, K. Leus, G. Wang, H. Chen, C. Jia, P. Van Der Voort, Generating Catalytic Sites in UiO-66 through Defect Engineering, *ACS Appl. Mater. Interfaces* 13 (2021) 60715–60735, <https://doi.org/10.1021/acsami.1c13525>.
- [14] H. Wu, Y.S. Chua, V. Krungleviciute, M. Tyagi, P. Chen, T. Yildirim, W. Zhou, Unusual and highly tunable missing-linker defects in zirconium metal-organic framework UiO-66 and their important effects on gas adsorption, *J. Am. Chem. Soc.* 135 (2013) 10525–10532, <https://doi.org/10.1021/ja404514r>.
- [15] A.H. Valekar, M. Lee, J.W. Yoon, J. Kwak, D.Y. Hong, K.R. Oh, G.Y. Cha, Y. U. Kwon, J. Jung, J.S. Chang, Y.K. Hwang, Catalytic transfer hydrogenation of furfural to furfuryl alcohol under mild conditions over Zr-MOFs: exploring the role of metal node coordination and modification, *ACS Catal.* 10 (2020) 3720–3732, <https://doi.org/10.1021/acscatal.9b05085>.
- [16] Z. An, J. Li, Recent advances in the catalytic transfer hydrogenation of furfural to furfuryl alcohol over heterogeneous catalysts, *Green. Chem.* 24 (2022) 1780–1808, <https://doi.org/10.1039/d1gc04440k>.
- [17] H. Xu, X. Song, M. Chen, W. Bai, M. Ji, Rigid confined space in Frustrated Lewis Pair/MOF catalyst: highly regioselective hydrogenation performance for α ,

- β -unsaturated carbonyl compounds, *J. Catal.* 421 (2023) 342–350, <https://doi.org/10.1016/j.jcat.2023.03.005>.
- [18] J. Ye, J.K. Johnson, Screening Lewis Pair Moieties for Catalytic Hydrogenation of CO₂ in Functionalized UiO-66, *ACS Catal.* 5 (2015) 6219–6229, <https://doi.org/10.1021/acscatal.5b01191>.
 - [19] J. Ye, J.K. Johnson, Design of Lewis Pair-Functionalized Metal Organic Frameworks for CO₂ Hydrogenation, *ACS Catal.* 5 (2015) 2921–2928, <https://doi.org/10.1021/acscatal.5b00396>.
 - [20] H. Cui, L. Zhong, X. Liao, F. Hao, W. Xiong, H. Liu, H. Luo, P. Liu, Y. Lv, Highly efficient chemoselective hydrogenation of unsaturated aldehydes catalyzed by hydrophobically modified core-shell defective ZIFs: Frustrated Lewis pair catalysis, *J. Catal.* 420 (2023) 23–43, <https://doi.org/10.1016/j.jcat.2023.02.012>.
 - [21] J.H. Cavka, S. Jakobsen, U. Olsbye, N. Guillou, C. Lamberti, S. Bordiga, K. P. Lillerud, A new zirconium inorganic building brick forming metal organic frameworks with exceptional stability, *J. Am. Chem. Soc.* 130 (2008) 13850–13851, <https://doi.org/10.1021/ja8057953>.
 - [22] H. Xu, M. Chen, M. Ji, Solid Lewis acid-base pair catalysts constructed by regulations on defects of UiO-66 for the catalytic hydrogenation of cinnamaldehyde, *Catal. Today* 402 (2022) 52–59, <https://doi.org/10.1016/j.cattod.2022.03.001>.
 - [23] K. Yang, J. Jiang, Computational design of a metal-based frustrated Lewis pair on defective UiO-66 for CO₂ hydrogenation to methanol, *J. Mater. Chem. A* 8 (2020) 22802–22815, <https://doi.org/10.1039/d0ta07051c>.
 - [24] P. Ponchai, K. Adpakpang, S. Thongratkaew, K. Chaipojjana, S. Wannapaiboon, S. Siwaipram, K. Faungnawakij, S. Bureekaew, Engineering zirconium-based UiO-66 for effective chemical conversion of d-xylose to lactic acid in aqueous condition, *Chem. Commun.* 56 (2020) 8019–8022, <https://doi.org/10.1039/d0cc03424j>.
 - [25] M. Qiu, T. Guo, R. Xi, D. Li, X. Qi, Highly efficient catalytic transfer hydrogenation of biomass-derived furfural to furfuryl alcohol using UiO-66 without metal catalysts, *Appl. Catal. A Gen.* 602 (2020), <https://doi.org/10.1016/j.apcata.2020.117719>.
 - [26] P. Yang, F. Mao, Y. Li, Q. Zhuang, J. Gu, Hierarchical porous Zr-Based MOFs synthesized by a facile monocarboxylic acid etching strategy, *Chem. - A Eur. J.* 24 (2018) 2962–2970, <https://doi.org/10.1002/chem.201705020>.
 - [27] L. Liu, Z. Chen, J. Wang, D. Zhang, Y. Zhu, S. Ling, K.W. Huang, Y. Belmabkhout, K. Adil, Y. Zhang, B. Slater, M. Eddaoudi, Y. Han, Imaging defects and their evolution in a metal-organic framework at sub-unit-cell resolution, *Nat. Chem.* 11 (2019) 622–628, <https://doi.org/10.1038/s41557-019-0263-4>.
 - [28] E. Plessers, D.E. De Vos, M.B.J. Roeffaers, Chemoselective reduction of α,β -unsaturated carbonyl compounds with UiO-66 materials, *J. Catal.* 340 (2016) 136–143, <https://doi.org/10.1016/j.jcat.2016.05.013>.
 - [29] H. Cui, S. Liu, Y. Lv, S. Wu, L. Wang, F. Hao, P. Liu, W. Xiong, H. Luo, Transfer hydrogenation of cinnamaldehyde to cinnamyl alcohol in hydrophobically modified core-shell MOFs nanoreactor: Identification of the formed metal-N as the structure of an active site, *J. Catal.* 381 (2020) 468–481, <https://doi.org/10.1016/j.jcat.2019.11.024>.
 - [30] Y. Zhang, X. Zheng, X. Guo, J. Zhang, A. Yuan, Y. Du, F. Gao, Design of modified MOFs electrocatalysts for water splitting: High current density operation and long-term stability, *Appl. Catal. B Environ.* 336 (2023), 122891, <https://doi.org/10.1016/j.apcatb.2023.122891>.
 - [31] A. Chhettry, Z. Wang, J. Hsu, J.L. Fox, A.A. Baig, A.M. Barry, H. Zhuang, M. Otsuka, W.I. Higuchi, Metastable equilibrium solubility distribution of carbonated apatite as a function of solution composition, *J. Colloid Interface Sci.* 218 (1999) 57–67, <https://doi.org/10.1006/jcis.1999.6384>.
 - [32] G.C. Shearer, S. Chavan, J. Ethiraj, J.G. Vitillo, S. Svelle, U. Olsbye, C. Lamberti, S. Bordiga, K.P. Lillerud, Tuned to perfection: Ironing out the defects in metal-organic framework UiO-66, *Chem. Mater.* 26 (2014) 4068–4071, <https://doi.org/10.1021/cm501859p>.
 - [33] H.G.T. Nguyen, N.M. Schweitzer, C.Y. Chang, T.L. Drake, M.C. So, P.C. Stair, O. K. Farha, J.T. Hupp, S.T. Nguyen, Vanadium-node-functionalized UiO-66: A thermally stable MOF-supported catalyst for the gas-phase oxidative dehydrogenation of cyclohexene, *ACS Catal.* 4 (2014) 2496–2500, <https://doi.org/10.1021/cs5001448>.
 - [34] S. Chaemchuen, Z. Luo, K. Zhou, B. Mousavi, S. Phatanasri, M. Jaroniec, F. Verpoort, Defect formation in metal-organic frameworks initiated by the crystal growth-rate and effect on catalytic performance, *J. Catal.* 354 (2017) 84–91, <https://doi.org/10.1016/j.jcat.2017.08.012>.
 - [35] A.M. Ebrahim, T.J. Bandosz, Ce(III) doped Zr-based MOFs as excellent NO₂ adsorbents at ambient conditions, *ACS Appl. Mater. Interfaces* 5 (2013) 10565–10573, <https://doi.org/10.1021/am402305u>.
 - [36] Y. Fan, H. Zhang, M. Ren, Y. Zhang, Y. Li, L. Wang, J. Chen, Low-temperature catalytic degradation of chlorinated aromatic hydrocarbons over bimetallic Ce-Zr/UiO-66 catalysts, *Chem. Eng. J.* 414 (2021), <https://doi.org/10.1016/j.cej.2021.128782>.
 - [37] S. Dai, Y. Chen, J. Yang, F. He, C. Chen, H. Xie, Surface treatment of nanozirconia fillers to strengthen dental bisphenol A-glycidyl methacrylate-based resin composites, *Int. J. Nanomed.* 14 (2019) 9185–9197, <https://doi.org/10.2147/IJN.1223392>.
 - [38] A. Vimont, J.M. Goupil, J.C. Lavalley, M. Daturi, S. Surblé, C. Serre, F. Millange, G. Férey, N. Audebrand, Investigation of acid sites in a zeotypic giant pores chromium(III) carboxylate, *J. Am. Chem. Soc.* 128 (2006) 3218–3227, <https://doi.org/10.1021/ja056906s>.
 - [39] K.R. Oh, A.H. Valekar, G.Y. Cha, Y. Kim, S.K. Lee, S.E. Sivan, P.P. Upare, M.J. Lee, Y.U. Kwon, Y.K. Hwang, In situ synthesis of trimeric ruthenium cluster-encapsulated ZIF-11 and its carbon derivatives for simultaneous conversion of glycerol and CO₂, *Chem. Mater.* 32 (2020) 10084–10095, <https://doi.org/10.1021/acs.chemmater.0c03423>.
 - [40] K.K. Ghuman, L.B. Hoch, T.E. Wood, C. Mims, C.V. Singh, G.A. Ozin, Surface analogues of molecular Frustrated Lewis Pairs in heterogeneous CO₂ hydrogenation catalysis, *ACS Catal.* 6 (2016) 5764–5770, <https://doi.org/10.1021/acscatal.6b01015>.
 - [41] K. Hadjiivanov, H. Knözinger, Characterization of vacant coordination sites of cations on the surfaces of oxides and zeolites using infrared spectroscopy of adsorbed probe molecules, *Surf. Sci.* 603 (2009) 1629–1636, <https://doi.org/10.1016/j.susc.2008.09.052>.
 - [42] M. Zhang, J. Zhang, Y. Wu, J. Pan, Q. Zhang, Y. Tan, Y. Han, Insight into the effects of the oxygen species over Ni/ZrO₂ catalyst surface on methane reforming with carbon dioxide, *Appl. Catal. B Environ.* 244 (2019) 427–437, <https://doi.org/10.1016/j.apcatb.2018.11.068>.
 - [43] A.G. Sato, D.P. Volanti, D.M. Meira, S. Damyanova, E. Longo, J.M.C. Bueno, Effect of the ZrO₂ phase on the structure and behavior of supported Cu catalysts for ethanol conversion, *J. Catal.* 307 (2013) 1–17, <https://doi.org/10.1016/j.jcat.2013.06.022>.
 - [44] S. Nong, W. Dong, Y. Xiao, M.S. Riaz, C. Dong, Y. Zhao, Z. Liu, R. Wang, F. Huang, Highly Hydroxylated Porous Nanozirconia for Complete Trace Cr(VI) Removal, *ACS Appl. Nano Mater.* 3 (2020) 3315–3322, <https://doi.org/10.1021/acsnm.0c00017>.
 - [45] D.M. Driscoll, D. Troya, P.M. Usov, A.J. Maynes, A.J. Morris, J.R. Morris, Characterization of Undercoordinated Zr Defect Sites in UiO-66 with Vibrational Spectroscopy of Adsorbed CO, *J. Phys. Chem. C* 122 (2018) 14582–14589, <https://doi.org/10.1021/acs.jpcc.8b03283>.
 - [46] A.D. Wiersum, E. Soubeyrand-Lenoir, Q. Yang, B. Moulin, V. Guillerme, M. Ben Yahia, S. Bourrelly, A. Vimont, S. Miller, C. Vagner, M. Daturi, G. Clet, C. Serre, G. Maurin, P.L. Llewellyn, An evaluation of UiO-66 for gas-based applications, *Chem. - Asian J.* 6 (2011) 3270–3280, <https://doi.org/10.1002/asia.201100201>.
 - [47] W. Zhang, Z. Yang, H. Wang, L. Lu, D. Liu, T. Li, S. Yan, H. Qin, T. Yu, Z. Zou, Crystal facet-dependent frustrated Lewis pairs on dual-metal hydroxide for photocatalytic CO₂ reduction, *Appl. Catal. B Environ.* 300 (2022), <https://doi.org/10.1016/j.apcatb.2021.120748>.
 - [48] Q. Wang, J. Feng, L. Zheng, B. Wang, R. Bi, Y. He, H. Liu, D. Li, Interfacial structure-determined reaction pathway and selectivity for 5-(hydroxymethyl) furfural hydrogenation over Cu-based catalysts, *ACS Catal.* 10 (2020) 1353–1365, <https://doi.org/10.1021/acscatal.9b03630>.
 - [49] X. Meng, Y. Yang, L. Chen, M. Xu, X. Zhang, M. Wei, A control over hydrogenation selectivity of furfural via tuning exposed facet of Ni catalysts, *ACS Catal.* 9 (2019) 4226–4235, <https://doi.org/10.1021/acscatal.9b00238>.
 - [50] J. Ni, W. Leng, J. Mao, J. Wang, J. Lin, D. Jiang, X. Li, Tuning electron density of metal nickel by support defects in Ni/ZrO₂ for selective hydrogenation of fatty acids to alkanes and alcohols, *Appl. Catal. B Environ.* 253 (2019) 170–178, <https://doi.org/10.1016/j.apcatb.2019.04.043>.
 - [51] S. Wang, K. Yin, Y. Zhang, H. Liu, Glycerol hydrogenolysis to propylene glycol and ethylene glycol on zirconia supported noble metal catalysts, *ACS Catal.* 3 (2013) 2112–2121, <https://doi.org/10.1021/cs400486z>.
 - [52] H. Peng, T. Dong, L. Zhang, C. Wang, W. Liu, J. Bao, X. Wang, N. Zhang, Z. Wang, P. Wu, P. Zhang, S. Dai, Active and stable Pt-Ceria nanowires/silica shell catalyst: Design, formation mechanism and total oxidation of CO and toluene, *Appl. Catal. B Environ.* 256 (2019), 117807, <https://doi.org/10.1016/j.apcatb.2019.117807>.
 - [53] L. Huo, B. Liu, H. Li, B. Cao, X. Cui, H. X. pu, Fu, C. Jia, J. Zhang, Component synergy and armor protection induced superior catalytic activity and stability of ultrathin Co-Fe spinel nanosheets confined in mesoporous silica shells for ammonia decomposition reaction, *Appl. Catal. B Environ.* 253 (2019) 121–130, <https://doi.org/10.1016/j.apcatb.2019.04.053>.
 - [54] D. Göhl, A. Garg, P. Paciok, K.J.J. Mayrhofer, M. Heggen, Y. Shao-Horn, R. E. Dunin-Borkowski, Y. Román-Leshkov, M. Ledendecker, Engineering stable electrocatalysts by synergistic stabilization between carbide cores and Pt shells, *Nat. Mater.* 19 (2020) 287–291, <https://doi.org/10.1038/s41563-019-0555-5>.
 - [55] X. Cao, J. Zhao, F. Long, X. Zhang, J. Xu, J. Jiang, Al-modified Pd@mSiO₂ core-shell catalysts for the selective hydrodeoxygenation of fatty acid esters: Influence of catalyst structure and Al atoms incorporation, *Appl. Catal. B Environ.* 305 (2022), 121068, <https://doi.org/10.1016/j.apcatb.2022.121068>.
 - [56] C. Wu, Q. Liu, R. Chen, J. Liu, H. Zhang, R. Li, K. Takahashi, P. Liu, J. Wang, Fabrication of ZIF-8@SiO₂ Micro/Nano Hierarchical Superhydrophobic Surface on AZ31 Magnesium Alloy with Impressive Corrosion Resistance and Abrasion Resistance, *ACS Appl. Mater. Interfaces* 9 (2017) 11106–11115, <https://doi.org/10.1021/acsaami.6b16848>.
 - [57] G. Miao, D. Huang, X. Ren, X. Li, Z. Li, J. Xiao, Visible-light induced photocatalytic oxidative desulfurization using BiVO₄/C₃N₄@SiO₂ with air/cumene hydroperoxide under ambient conditions, *Appl. Catal. B Environ.* 192 (2016) 72–79, <https://doi.org/10.1016/j.apcatb.2016.03.033>.
 - [58] X. Zhang, C. Yang, P. An, C. Cui, Y. Ma, H. Liu, H. Wang, X. Yan, G. Li, Z. Tang, Creating enzyme-mimicking nanopockets in metal-organic frameworks for catalysis, *Sci. Adv.* 8 (2022), <https://doi.org/10.1126/sciadv.add5678>.
 - [59] J. Song, L. Wu, B. Zhou, H. Zhou, H. Fan, Y. Yang, Q. Meng, B. Han, A new porous Zr-containing catalyst with a phenate group: An efficient catalyst for the catalytic transfer hydrogenation of ethyl levulinate to γ -valerolactone, *Green. Chem.* 17 (2015) 1626–1632, <https://doi.org/10.1039/c4gc02104e>.